Nonlinear studies of binary black hole mergers in Einstein-scalar-Gauss-Bonnet gravity

Maxence Corman[1,2,*] Justin L. Ripley[3,4,†] and William E. East[1,‡]

[1]*Perimeter Institute for Theoretical Physics, Waterloo, Ontario N2L 2Y5, Canada*
[2]*Department of Physics and Astronomy, University of Waterloo, Waterloo, Ontario N2L 3G1, Canada*
[3]*Illinois Center for Advanced Studies of the Universe and Department of Physics,*
University of Illinois at Urbana-Champaign, Urbana, Illinois 61801, USA
[4]*DAMTP, Centre for Mathematical Sciences, University of Cambridge,*
Wilberforce Road, Cambridge CB3 0WA, United Kingdom

We study the nonlinear dynamics of binary black hole systems with scalar charge by numerically evolving the full equations of motion for shift-symmetric Einstein scalar Gauss-Bonnet gravity. We consider quasicircular binaries with different mass-ratios, varying the Gauss-Bonnet coupling and quantifying its impact on the emitted scalar and gravitational waves. We compare our numerical results to post-Newtonian calculations of the radiation emitted during the inspiral. We demonstrate the accuracy of the leading-order terms in post-Newtonian theory in modeling the amplitude of the scalar waveform, but find that, at least for the last few orbits before merger, the currently available post-Newtonian theory is not sufficient to model the dephasing of the gravitational wave signal in this theory. We further find that there is non-negligible nonlinear enhancement in the scalar field at merger, but that the effect on the peak gravitational wave emission is small.

I. INTRODUCTION

In recent years, the gravitational waves (GW) observed from the inspiral, merger, and ringdown of black hole binaries have greatly constrained the landscape of potential deviations from General Relativity (GR) [1–11]. However, in order to seek physics beyond GR, or to place the most stringent constraints on deformations of GR, one needs accurate predictions for specific modified gravity theories, in particular in the strong field and dynamical regime [12–15]. This has been a major theoretical and technical challenge for many theories of interest [16–25]. As a result, most tests of GR performed so far are model-independent or null tests, more commonly classified as consistency and parametrized tests [4,26–29]. Parametrized tests introduce deviations from GR to the gravitational waveform in a theory-agnostic way, and use the data to constrain the beyond GR parameters. Most current approaches, however, usually only constrain the deviations by considering one specific modification at a time and thus the interpretation of these constraints remains limited.

An interesting class of theories to test against GR is Einstein-scalar-Gauss-Bonnet (ESGB) gravity, which introduces modifications to GR at small curvature length scales. Variants of ESGB gravity allow for scalar-charged black holes [30–33], and hence can differ qualitatively from GR in the strong field regime, while still passing weak field tests. Because of this, much recent work has gone into modeling compact object mergers in ESGB gravity in both post-Newtonian (PN) theory [34–37] and numerical relativity [19,22,23,38–40]. In Ref. [22], two of us introduced a computational methodology to solve the equations of motion for binary black hole system in ESGB gravity without approximation (beyond that of numerical truncation error), by making use of the modified generalized harmonic (MGH) formulation [41,42].[1] Here we follow up on that work, and study the dynamics of the last stages of the inspiral phase of quasicircular, nonspinning black holes in shift-symmetric ESGB (sGB) gravity, and investigate the accuracy of PN approximations [34–37].

In general, the equations of motion for ESGB gravity can only be stably evolved in time for weakly-coupled solutions [22,23,41,42,44]. Weak coupling roughly means that the Gauss-Bonnet corrections to the spacetime geometry remain sufficiently small compared to the smallest curvature length scale in the solution. A binary black hole system in ESGB gravity can evolve from an initially

*[*]mcorman@perimeterinstitute.ca
[†]ripley@illinois.edu
[‡]weast@perimeterinstitute.ca

---

[1]These methods were recently extended to a modified version of the CCZ4 formulation in Ref. [43].

weakly coupled state to a strongly coupled state, as the black holes become closer and eventually merge [45,46]. We find that in a significant portion of the parameter space, our evolution breaks down as the black holes become closer, although approaching this limit does not appear to be preceded by dramatically different spacetime or scalar field dynamics compared to the weakly-coupled regime. Maintaining a weakly-coupled solution exterior to the black hole horizons through merger remains a major challenge in the numerical evolution of binary black holes in numerical relativity. While better addressing this issue remains an important issue for future work, for many cases here we focus on the properties of the late inspiral phase of binary evolution. Even when restricting to the inspiral phase, we show that the deviations from GR are significant in terms of the imprint on the resulting gravitational waves. One of our main results is that leading-order PN approximations are not sufficient to model the gravitational signal in the late stages of the inspiral. For the cases we were able to evolve through merger, we find that the effects of ESGB gravity show up primarily in an nonlinear enhancement of the scalar field at merger, and in the dephasing of the gravitational waves, while the effect on the peak amplitude of the gravitational wave signal is small. This work also demonstrates the efficacy of the numerical relativity techniques utilized here—which should be applicable to any scalar-tensor theory with second-order equations of motion—to quantify the impact on the gravitational wave signal of modified gravity in regimes where other approximations break down.

The remainder of the paper is as follows. In Sec. II, we review shift-symmetric ESGB gravity. In Sec. III, we describe our numerical methods for evolving this theory and analyzing the results. Results from our study of quasicircular binary black holes in sGB are presented in Sec. IV. We discuss these results and conclude in Sec. V. We discuss the accuracy of our simulations in Appendix A, collect PN results in sGB in Sec. B, outline our initial-data setup in Appendix C, and review the accuracy of the perturbative approach to solving the equations of motion in Appendix D. We use geometric units: $G = c = 1$, a metric sign convention of $-+++$, lower case Latin letters to index spacetime indices, and lower case Greek letters to index spatial indices. The Riemann tensor is $R^a{}_{bcd} = \partial_c \Gamma^a_{db} - \cdots$.

II. SHIFT-SYMMETRIC ESGB GRAVITY

We briefly review shift-symmetric ESGB (sGB) gravity. The action is

$$S = \frac{1}{16\pi} \int d^4x \sqrt{-g}(R - (\nabla\phi)^2 + 2\lambda\phi\mathcal{G}), \quad (1)$$

where $\mathcal{G}$ is the Gauss-Bonnet scalar

$$\mathcal{G} \equiv R^2 - 4R_{ab}R^{ab} + R_{abcd}R^{abcd}. \quad (2)$$

Here, λ is a constant coupling parameter that, in geometric units, has dimensions of length squared. As the Gauss-Bonnet scalar $\mathcal{G}$ is a total derivative in four dimensions, we see that the action of sGB gravity is preserved up to total derivatives under constant shifts in the scalar field: $\phi \to \phi + \text{constant}$. Schwarzschild and Kerr black holes are not stationary solutions in this theory; if one begins with such vacuum initial data, the black holes will dynamically develop stable scalar clouds (hair). The end state then is a scalar-charged black hole, so long as the coupling normalized by the black hole mass m, λ/m^2, is sufficiently small [22,32,33,47]. In particular, regularity of black hole solutions and hyperbolicity of the theory sets $\lambda/m^2 \lesssim 0.23$ for nonspinning black holes, [33,47]. In contrast to stars, where the scalar field around them falls of more rapidly than $1/r$, black holes have a scalar charge, and thus black hole binaries emit scalar radiation, which increases the speed at which the binary inspirals and merges [34,48]. The most stringent observational bounds on the theory come from unequal mass, or black hole-star binaries, as those emit scalar dipole radiation, which leads to a more rapid dephasing of the gravitational waveform than would be observed in GR. In PN theory, the scalar dipole radiation enters as a -1 PN effect and can dominate over gravitational radiation at sufficiently wide separations (low frequencies). In this study, we will focus on late inspiral, where the gravitational waves are strongest and the scalar radiation is subdominant (the quadrupolar driven inspiral regime). Another feature of these solutions is that the scalar charge is inversely proportional to the square of the smallest mass black hole in the system. This suggests that the best way to probe EsGB gravity is by observing the smallest compact objects. We therefore expect stronger constraints on the theory will come from observing the merger of stellar mass black holes with ground-based detectors, as opposed to observations of supermassive black hole mergers with LISA (although long-duration observations of extreme mass-ratio insipirals with LISA may provide meaningful constraints [49]). Restoring dimensions, comparisons of gravitational wave observations from the LIGO-Virgo-KAGRA catalogue to PN results place constraints of $\sqrt{\lambda} \lesssim 2.5$ km, see Refs. [50,51].

III. METHODS

A. Evolution equations and code overview

The covariant equations of motion for sGB gravity are

$$\Box\phi + \lambda\mathcal{G} = 0, \quad (3)$$

$$R_{ab} - \frac{1}{2}g_{ab}R - \nabla_a\phi\nabla_b\phi + \frac{1}{2}(\nabla\phi)^2 g_{ab}$$
$$+ 2\lambda\delta^{efcd}_{ijg(a}g_{b)d}R^{ij}{}_{ef}\nabla^g\nabla_c\phi = 0, \quad (4)$$

where δ_{efgh}^{abcd} is the generalized Kronecker delta tensor. We numerically evolve the full sGB equations of motion using the MGH formulation [41,42]. We use similar choices for the gauge and numerical parameters as in Ref. [22]. We worked with box-in-box adaptive mesh refinement as provided by the PAMR library [52]. We typically worked with eight levels of mesh refinement in our simulations, unless otherwise noted. We provide details on numerical resolution and convergence in Appendix A.

B. Puncture binary black hole initial data

On our initial time slice, we must satisfy the generalizations of the Hamiltonian and momentum constraint equations to sGB. Here, we do not implement a method to solve the equations for general ϕ, but instead consider initial data for which $\phi = \partial_t \phi = 0$. With this choice of ϕ, the constraint equations of sGB gravity reduce to those of vacuum GR [22,23]. Even though $\phi = \partial_t \phi = 0$ on the initial time slice, scalar field clouds subsequently form on a timescale that is short compared with the orbital binary timescale (within $\sim 100 M_0$). We construct quasicircular binary black hole initial data via the black hole puncture method [53], using the `TwoPunctures` code [54,55] (footnote 3).

For puncture binary black hole initial data, we need to specify the initial black hole positions, and their approximate initial masses $m_{1,2}$ (with the convention that $m_1 \leq m_2$), linear momenta $P_{1,2}^\gamma$, and spins $S_{1,2}^\gamma$ (which we set to zero in this study). Given $m_{1,2}$ and the initial puncture (black hole) locations, we use the dynamics for a circular binary to 2PN order to determine the tangential components to $P_{1,2}^\gamma$, and the 2.5PN radiation reaction term to determine the initial radial component of $P_{1,2}^\gamma$ [56]. We review our initial data setup in more detail in Appendix C.

For the first $t = 50 M_0$ (where $M_0 \equiv m_1 + m_2$) of evolution, we evolve the black holes purely in GR. We found this allowed for the junk radiation from the puncture initial data to disperse away from the black holes. After that initial evolution time, we turn on the Gauss-Bonnet coupling λ to a nonzero value. The constraints are satisfied in this procedure, as we can think of our initial data as starting at $t = 50 M_0$ instead, with $\phi = \partial_t \phi = 0$ and a metric field that satisfies the constraints such that the initial data satisfies the constraint equations for sGB gravity [22,23]. While we use quasicircular initial data based on PN approximations for the initial orbital velocities from GR, we found that the scalarization process does not appreciably impact the eccentricity of our runs, and instead the eccentricity of our runs is dominated by the truncation error of the simulations. For more discussion, see Appendix A.

C. Diagnostic quantities

We use many of the same diagnostics as in Ref. [22], which we briefly review here. We measure the scalar and gravitational radiation by extracting the scalar field ϕ and Newman-Penrose scalar Ψ_4 on finite-radius coordinate spheres. Due to the coupling between the scalar field and metric through the Gauss-Bonnet coupling, in general scalar and gravitational radiation will couple together through the term $\delta \times \text{Riemm} \times \nabla\nabla\phi$. For asymptotically flat spacetimes that have an asymptotically flat future null infinity (that is spacetimes for which the peeling theorem holds, so the Weyl scalar fall of sufficiently fast [57]), this coupling falls off as $1/r^4$ as $r \to \infty$. For those spacetimes, in the wave zone, we can treat the gravitational and scalar radiation as two uncoupled quantities (for related discussions, see [22,58]). We discuss how we estimate the finite-radius extraction error of our waveforms in Appendix A.

We decompose Ψ_4 and ϕ into their spin-weighted spherical harmonic components

$$\Psi_{4,\ell m}(t,r) \equiv \int_{\mathbb{S}_2} {}_{-2}\bar{Y}_{\ell m}(\vartheta,\varphi)\Psi_4(t,r,\vartheta,\varphi), \quad (5a)$$

$$\phi_{\ell m}(t,r) \equiv \int_{\mathbb{S}_2} {}_{0}\bar{Y}_{\ell m}(\vartheta,\varphi)\phi(t,r,\vartheta,\varphi). \quad (5b)$$

The gravitational wave luminosity is

$$P_{\text{GW}}(t) = \lim_{r\to\infty} \frac{r^2}{16\pi} \int_{\mathbb{S}_2} \left| \int_{-\infty}^{t} \Psi_4 \right|^2. \quad (6)$$

The scalar wave luminosity is P_{SF}

$$P_{\text{SF}} \equiv -\lim_{r\to\infty} r^2 \int_{\mathbb{S}_2} N t^a (T^{\text{SF}})_a^b dA_b, \quad (7)$$

where $N = 1/\sqrt{-g^{tt}}$ is the lapse and t^a is the asymptotic timelike Killing vector, the integral is over a sphere, and

$$T_{ab}^{\text{SF}} \equiv \frac{1}{8\pi}\left(\nabla_a\phi\nabla_b\phi - \frac{1}{2}g_{ab}\nabla_c\phi\nabla^c\phi\right). \quad (8)$$

We assume the scalar radiation is outgoing, so that Eq. (7) reduces to

$$P_{\text{SF}}(t) = \lim_{r\to\infty} \frac{r^2}{8\pi} \int_{\mathbb{S}_2} (\partial_t\phi)^2. \quad (9)$$

To compare our numerical waveforms, we must estimate the orbital frequency of the binary Ω. We do so using the approximate relation [59–61]

$$\Omega \approx \frac{1}{2}\frac{d\Phi_{22}(t)}{dt}, \quad (10)$$

where $\Phi_{22}/2$ is the definition of orbital phase computed from half the complex phase of $\Psi_{4,22}$. We track the apparent horizons (AHs) associated with the black holes, and measure their areas and associated angular momentum J_{BH}.

From this, we compute the black hole mass m_{BH} via the Christodoulou formula [62]

$$m_{BH} \equiv \sqrt{M_A^2 + \frac{J_{AH}^2}{4M_A^2}}, \qquad (11)$$

where $M_A \equiv \sqrt{\mathcal{A}/(16\pi)}$ is the areal mass. We note that while the areal mass always increases in vacuum GR [63], it can decrease in sGB gravity as the theory can violate the null convergence condition (which is $R_{ab}k^a k^b \geq 0$ for all null k^a) [44,47]. In our simulations, $J_{AH} \approx 0$ to numerical precision for the constituents of the binary black hole. We measure the average value of the scalar field on the black hole apparent horizons

$$\langle \phi \rangle_{AH} \equiv \frac{1}{\mathcal{A}} \int_{AH} \phi. \qquad (12)$$

D. Cases considered

We focus on quasicircular black hole binaries with no spin. We classify our runs by two dimensionless numbers; their mass ratio q and by the relative Gauss-Bonnet scalar coupling strength ζ_1 (compare to Refs. [34,50,51])

$$q \equiv \frac{m_1}{m_2} \leq 1, \qquad \zeta_1 \equiv \frac{\lambda}{m_1^2}. \qquad (13)$$

As m_1 is the smaller black hole mass, it roughly quantifies the smallest curvature scale in our simulations. We consider the mass ratios $q = 1$, $2/3$, and $1/2$, with an initial separation of $10M_0$, approximately 8 orbits before merger in GR. For the equal mass ratios, we consider ESGB coupling parameters $\zeta_1 = 0$, 0.01, 0.05, and 0.1; while for the mass ratios $q = 2/3$ and $q = 1/2$, we consider smaller values of $\zeta_1 = 0$, 0.025, 0.05, and 0.075; and $\zeta_1 = 0$, 0.05, and 0.075, respectively. When comparing waveforms ($\Psi_{4,\ell m}$ or $\phi_{\ell m}$) with different values of the coupling, we compute the time t_{align} at which the gravitational wave frequency is $0.01M_0$, and apply this as a time offset. This alleviates the effect of any dephasing or shift in frequency due to the scalarization process. We then rotate the waveforms by a constant, complex phase so that their initial phases align. For comparisons with other works, our coupling λ corresponds to $\alpha_{GB} \equiv \lambda/\sqrt{8\pi}$ used in, e.g., [50,51].[2] Restoring physical units, we have

$$\sqrt{\alpha_{GB}} \approx 3.97 \text{ km} \left(\frac{\sqrt{\lambda}}{m_1} \right) \left(\frac{m_1}{6M_\odot} \right), \qquad (14)$$

where $6M_\odot$ is approximately the value of smallest black hole observed in the LIGO-Virgo-Kagra third observing run [67].

---

[2]However, several other studies (e.g., [38,64–66]) take conventions leading to a value of α_{GB} that is $16\sqrt{\pi}\times$ times larger.

For reference, Ref. [51] sets a constraint of $\sqrt{\alpha_{GB}} \lesssim 1.2$ km by comparing gravitational wave observations of black hole-neutron star binaries to PN results of ESGB. In comparison, the largest coupling we consider in our simulations (our equal-mass $\zeta = 0.1$ run) corresponds to $\sqrt{\alpha_{GB}} \sim 1.25$ km for a $6M_\odot$ black hole, which is roughly within observational bounds.

E. Challenges in modeling the merger phase of black hole evolution

As we discuss in Sec. IV, we are unable to evolve the binaries through merger for many of our simulations. For some of our runs, we turned off the scalar Gauss-Bonnet coupling inside a compact ellipsoidal region centered at the black hole binaries center of mass at a finite time before merger. This allowed us to evolve through merger, and extract gravitational and scalar radiation from the inspiral up until the causal future of the excised region intersected where we measured the radiation (typically at $r/M_0 = 90$).

For one case, namely $q = 1$ and $\zeta_1 = 0.05$, we only turn off the Gauss-Bonnet coupling slightly before finding a common apparent horizon, and only in a localized region that is encompassed by the final black hole. We have verified that varying the size of this region has no appreciable impact on the resulting radiation, and so we include the full results from this case, though a careful tracking of the propagation of information along characteristics would be needed to more rigorously justify this.

We believe the main difficulty with evolving through merger in our simulations may be elliptic regions that form around merger. These regions may possibly be hidden behind the final event horizon, and so could possibly be excised from the computational domain if an apparent horizon is located quickly enough. Higher-resolution runs, with excision surfaces that lie closer to the apparent horizons of the inspiraling black holes or a different choice of the auxiliary metrics in the modified generalized harmonic formulation, may allow for the successful merger of black holes in sGB gravity with unequal mass ratios. We leave a further investigation of this to future work.

IV. RESULTS

We present results for binary black holes with several mass ratios, beginning roughly eight orbits before merger, focusing on how the orbital dynamics and radiation changes as a function of the sGB coupling. We compare both the scalar radiation, and the modified gravity induced dephasing of the orbit and gravitational wave signal to the PN prediction.

A. Scalar radiation and dynamics

In Fig. 1, we compare the leading-order scalar waveforms $\phi_{\ell m}$ from our numerical evolution to the PN formulas given in Eq. (B1). The PN formulas are accurate

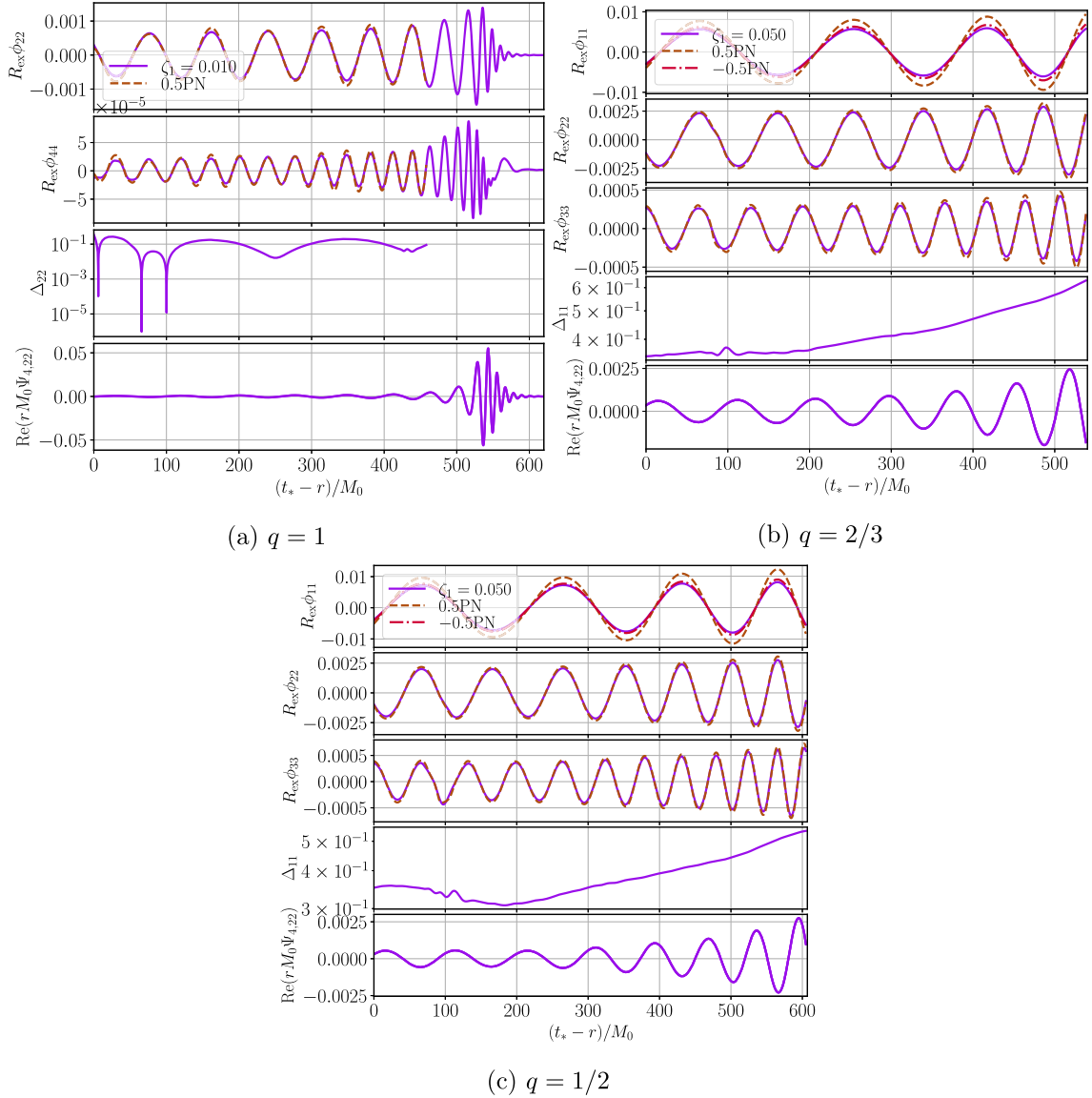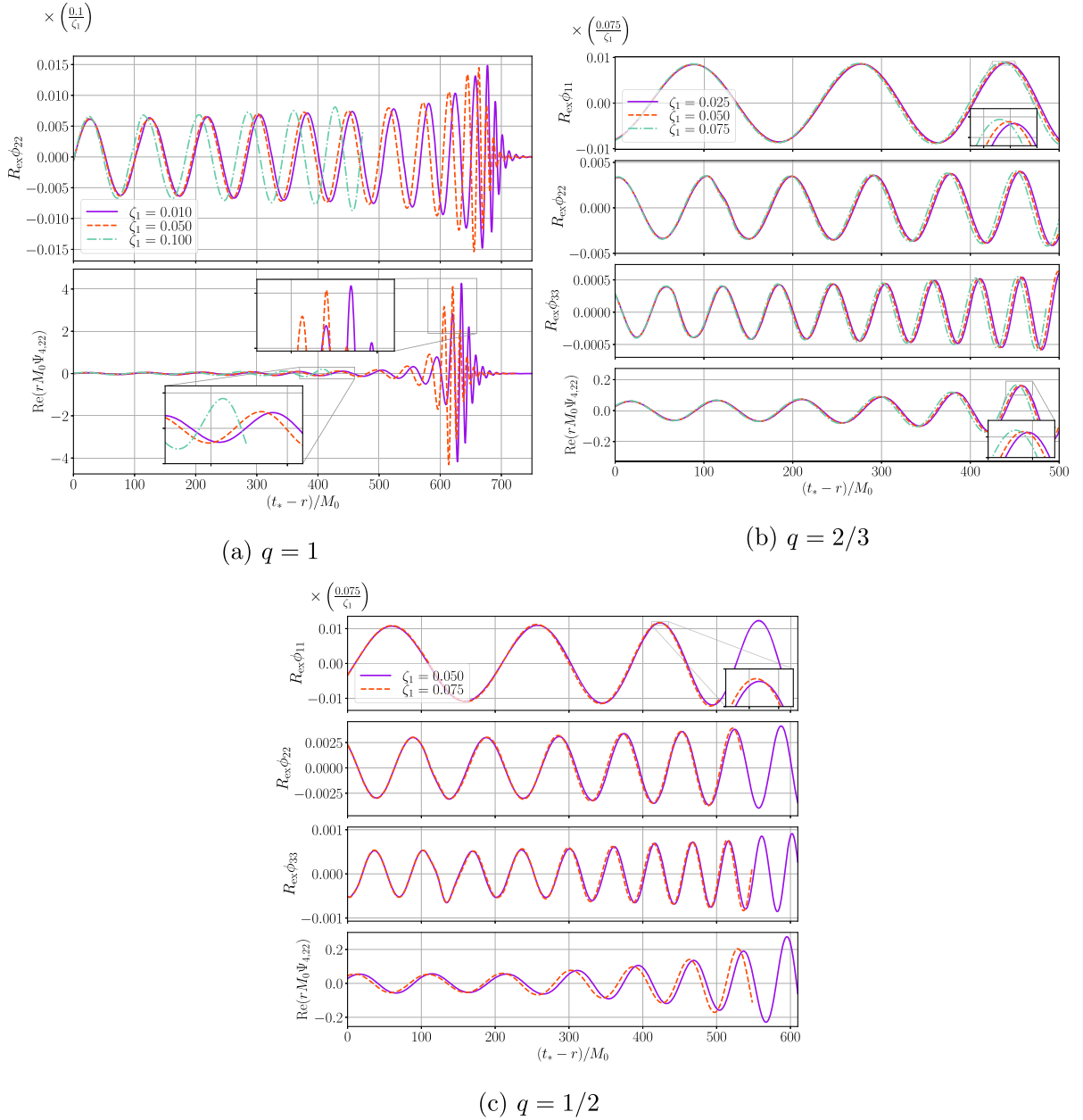(a) $q = 1$

(b) $q = 2/3$

(c) $q = 1/2$

FIG. 1. Scalar waveforms as a function of retarded time, $t_* - r = t - t_{\text{align}} - r$, rescaled by the extraction radius $R_{\text{ex}} = r/M_0 = 90$, sourced by nonspinning BH binaries of mass ratio $q = \{1, 2/3, 1/2\}$ (clockwise from the top left). The corresponding waveform $\Psi_{4,22}$ is displayed in the bottom for comparison. We show the $(\ell, m) = (2, 2)$ and $(4, 4)$ spherical harmonic components for the equal mass ratio and the $(\ell, m) = (1, 1)$, $(2, 2)$, and $(3, 3)$ components for unequal mass ratios. During the inspiral, we also display the PN waveform (brown dashed lines), derived to 0.5PN order, and the leading-order waveform at -0.5PN for the $(\ell, m) = (1, 1)$ mode (red dash-dotted lines). We also show the relative difference between the amplitude of the PN and numerical waveform Δ_{lm} for the leading-order mode.

to 0.5PN order for the mode ϕ_{11}, and to leading PN order for the remaining modes. As in the comparisons of scalar waveforms computed in Refs. [36–38], the frequency we use in the PN expressions are obtained from our numerical evolutions using Eq. (10), so our comparison is measuring the accuracy of the PN approximation in determining the amplitude of the scalar field, given its frequency. We see that the fractional difference between the 0.5PN order PN theory for the $\ell = 1$, $m = 1$ mode, and the numerical scalar waveform is about 30% initially, and grows as the binary inspirals. We also note that the inclusion of higher PN terms

increases the overall amplitude of the scalar waveforms, making the agreement between the PN and numerical waveforms worse than at leading order at the frequencies we consider. This result holds for all three mass ratios we considered. Comparing other values of the coupling constant shows similar behavior and thus, we do not show the plots here.

Comparing our results to Fig. 7 of Ref. [38], where the leading-order PN scalar waveforms were compared to numerical waveforms obtained in a test field approximation (valid to first order in the coupling parameter ζ_1),

FIG. 2. Scalar waveforms as a function of retarded time, $t_* - r = t - t_{align} - r$, rescaled by the extraction radius $R_{ex} = r/M_0 = 90$ and test field dependence on coupling constant λ, sourced by nonspinning binary black holes of mass ratio $q = \{1, 2/3, 1/2\}$ (clockwise from top left) and different coupling constants ζ_1. The corresponding gravitational waveforms $\Psi_{4,22}$ are displayed in the bottom of each panel for comparison. We show the leading-order (ℓ, m) mode for each mass ratio.

we find close agreement between our waveforms, suggesting the test field scalar waveform computed from a prescribed orbital evolution is fairly accurate at least during the early inspiral phase. This is further emphasized in Fig. 2, where we plot the scalar waveforms, rescaled by ζ_1. In the decoupling limit, the amplitude of the emitted waveforms is directly proportional to ζ_1 [34,38]. From Fig. 2, we see that, at least during the inspiral phase of binary black hole evolution, this relation holds up well for the full theory. This is to be expected, as nonlinear corrections to ϕ only enter at order ζ_1^3 in sGB gravity; see Appendix D.

In Fig. 3, we plot the average value of ϕ on the black hole apparent horizon for the two initial black holes, and the final remnant black hole, for runs with ($q = 1$, $\zeta_1 = 0.01$ and 0.05) and ($q = 1/2, \zeta_1 = 0.05$). We see that after the black holes have acquired a scalar charge, the average value of the scalar field on the two black hole horizons increases as they inspiral towards each other, in general qualitative agreement with the predictions of

(a) $q = 1, \zeta_1 = 0.01$ and 0.05
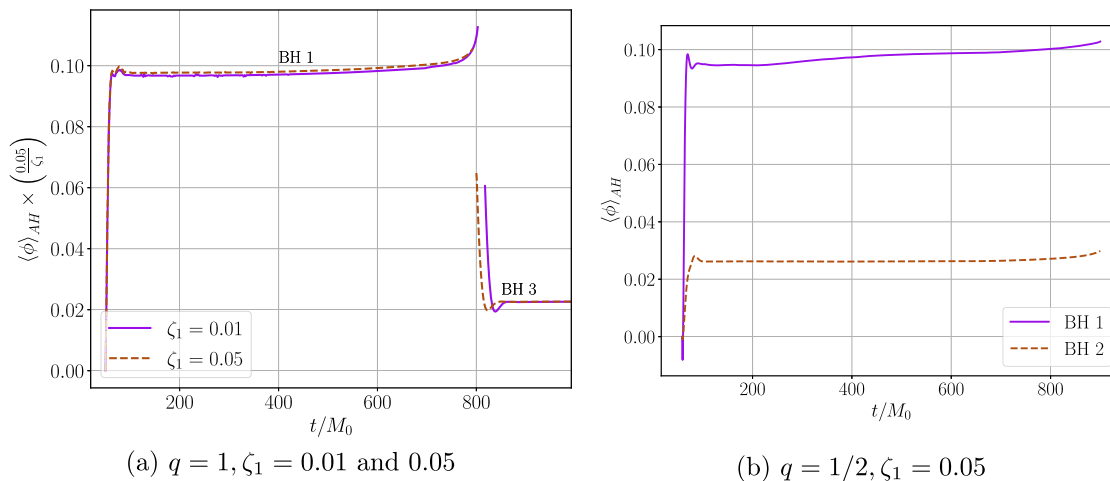
(b) $q = 1/2, \zeta_1 = 0.05$

FIG. 3. Average value of the scalar field, rescaled by the test field dependence, over the black hole horizons for different mass ratios. For the equal mass ratio binary (left panel), we were able to evolve through merger, and thus determine the average value of the scalar field on the third, remnant black hole. While we were unable to evolve through merger for the unequal mass ratio binaries, on the right panel we show the average scalar field for a $q = 1/2$ run. The dips in the average scalar field near the end of the evolution for that run are due to numerical error.

Refs. [45,46]. The remnant black hole for the equal mass runs (BH3 in the left panel) has a smaller average scalar field value on its horizon than the two original black holes, as it has a larger mass (so $\lambda/m_3^2 < \lambda/m_{1,2}^2$), and it is spinning [22]. As we discuss in Sec. III E, we are unable to evolve through merger for any of the unequal mass ratio cases we consider, so there is no remnant apparent horizon in the right panel.

B. Gravitational waves

We next estimate the relative dephasing of the gravitational waveforms, taking into account various sources of numerical error in our simulations. Accurately computing the phase of a gravitational signal is crucial, given this will be the most salient effect of sGB gravity that current gravitational wave detectors are able to measure [2,14,51]. Due to the presence of scalar charge around each black hole in sGB gravity, black holes will emit scalar radiation as they inspiral each other, so they will inspiral faster as compared to what would be the case in GR. In Fig. 4, we plot the gravitational waveforms $\Psi_{4,22}$, after matching their frequency at a time t_{align}, and applying a rotation in the complex plane, so that their phases align initially. We see that there is a noticeable dephasing of binaries with different values of ζ_1. In Fig. 5, we quantify the dephasing for the $\ell = 2$, $m = 2$ mode of Ψ_4 [see Eq. (A3)]

$$\delta\Phi(f) \equiv \Phi_{\text{sGB}}(f) - \Phi_{\text{GR}}(f), \qquad (15)$$

by comparing the orbital phase [computed from Eq. (A3)] of the waveforms at a given frequency smaller than $M_0 f < 0.018$ which corresponds to the empirically found transition from the inspiral to merger-ringdown phase in GR [68,69], along with the corresponding PN predictions for a quadrupolar driven inspiral [35,51] (see also Appendix B). We find $\delta\Phi < 0$, and the dephasing grows as we increase the coupling λ, which is in general qualitative agreement with PN predictions for sGB gravity. This being said, at least for the last few orbits of the inspiral that we study, we find that our results do not agree quantitatively with PN predictions. A possible reason for this is because we are comparing to PN theory close to the merger phase of binary evolution, where more orders of the PN expansion are needed to match to numerical relativity simulations even in GR. These differences also need to be compared to the various sources of numerical error in the simulations, which in some cases exceed the small phase differences, as we discuss below. In Fig. 6, we show the dephasing at consecutive orders up to 2PN for a range of gravitational wave frequencies we sample in our simulations (the last few orbits before merger), yet within the regime where the PN approximation should be valid in GR, $M_0 f < 0.018$ [68,69]. The PN formulas we plot were first presented including terms of up to 2PN order in Ref. [51]; we review their computation in Appendix B. As noted in Ref. [51], we mention that the dephasing for ESGB gravity has only been computed to 2PN order, with only partial results at 0.5PN order onwards. We see that there are still noticeable differences in the PN approximation with the addition of the highest-order terms in the near-merger regime studied here, and thus the expansion will likely have to be continued to higher order to achieve a highly accurate prediction in that regime, although we cannot rule out that the inclusion of the currently missing terms
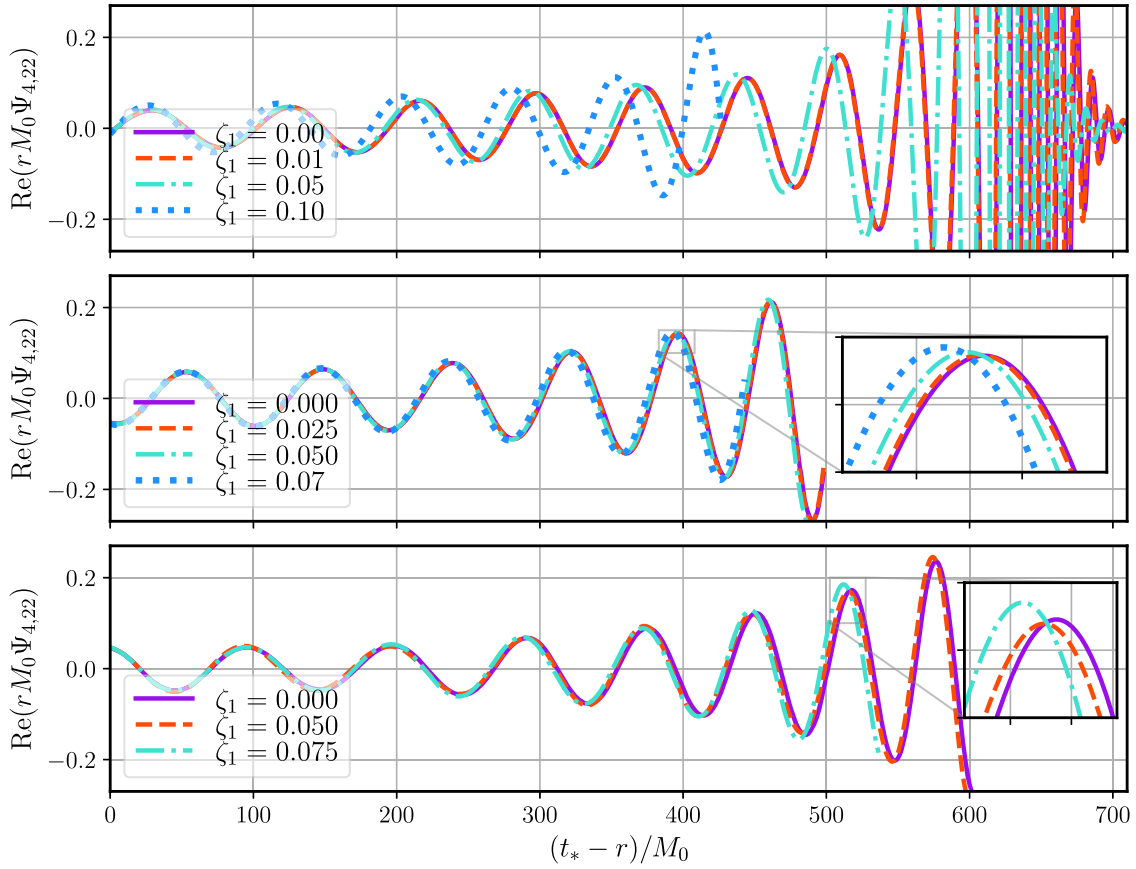
FIG. 4. The radially rescaled value of $\Psi_{4,22}$ as a function of retarded time, $t_* - r = t - t_{\text{align}} - r$, for different values of ζ_1. The top, middle, and bottom panels show the waveforms for the $q = 1$, $2/3$, and $1/2$ mass ratio binaries. Here we measure $\Psi_{4,22}$ at a radius of $R_{\text{ex}} = r/M_0 = 90$.

to the 0.5PN through 2PN contributions in the phase may lead to a faster convergence in the PN expansion than observed here.

Finally, we compare the orbital dephasing to the numerical errors in the simulations. A detailed error analysis is given in Appendix A, which we briefly summarize here.
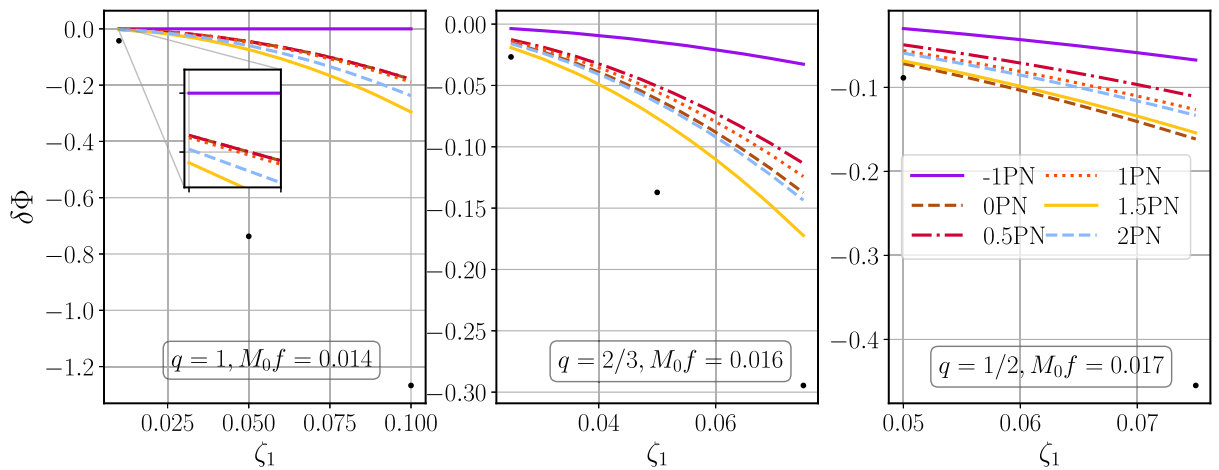
FIG. 5. Difference between the orbital phase of gravitational waveform in sGB and GR, $\delta\Phi$ [see Eq. (B3)], accumulated as the binary evolves from a frequency $f_0 = 0.01/M_0$ to a frequency f. The left, middle, and right panels display results for the $q = 1$, $2/3$, and $1/2$ mass ratio binaries, respectively, with $M_0 f = 0.014$, 0.016, and 0.017. We plot the PN predictions for orders -1PN through 2PN (with each curve including all terms up to that order).
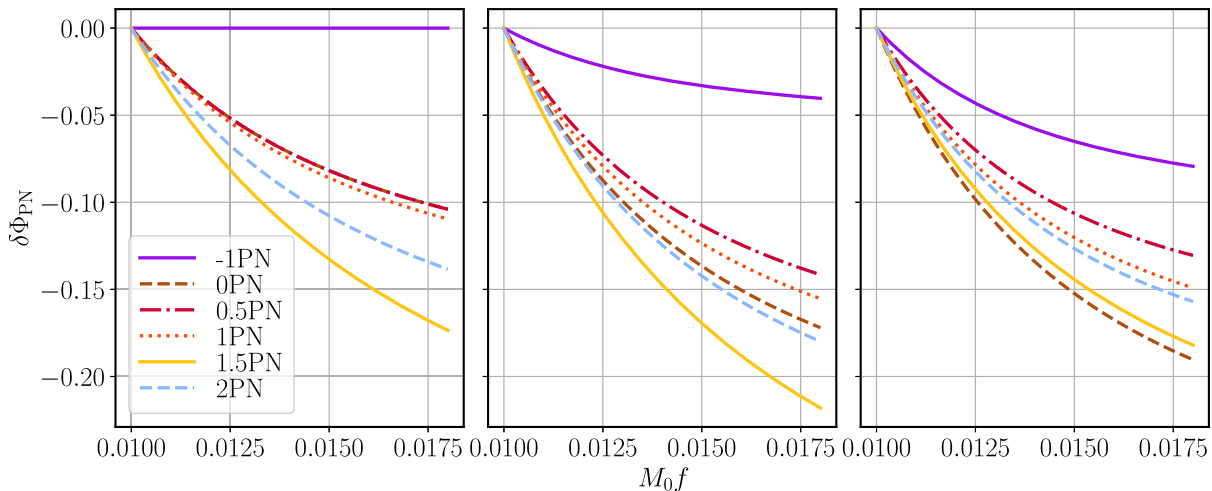
FIG. 6. The shift in the gravitational wave phase for the orbital phase, summed to each PN order up to 2PN. In the left, middle, and right panels we set $\zeta_1 = 0.05$, 0.075, and 0.075, respectively. As in Fig. 4, the left panel is for a $q = 1$ binary, the middle panel is for a $q = 2/3$ binary, and the right panel is for a $q = 1/2$ binary.

The error in the Richardson extrapolated phase is ~ 0.25 radians, which is comparable to the ESGB dephasing, and larger than the relative error in the 2PN computation. However, if the dominant truncation error in our simulations does not depend strongly on the value of ζ_1, and thus partially cancels out when calculating the difference $\delta \Phi$ in the phase between the sGB and GR simulations using the same resolution, this will lead to noticeable smaller truncation error in this quantity compared to the overall phase. We see evidence that this is the case, for example, by comparing a measure of the truncation error in $\delta \Phi$, computed by comparing a $q = 1/2$ GR simulation to an equivalent sGB simulation with $\zeta_1 = 0.075$ at two different resolutions, to an estimate of the overall truncation error in Φ for the same sGB case. We find the former to be $\sim 50 \times$ smaller than the latter (see Appendix A). We also find similar results for the GW amplitude. Thus, for a number of cases (see Fig. 5), the difference in errors is smaller than the dephasing $\delta \Phi$ we measure.

Lastly, we note that the dephasing between the sGB and GR simulations may be caused by small differences in the eccentricity of our simulations, which would be caused by the orbit being slightly perturbed by the rapid development of the scalar field around the black holes at early times, as an artifact of using initial conditions with $\phi = \partial_t \phi = 0$. If this were the case, one would expect the eccentricity of the modified waveforms to increase with coupling. We estimate the orbital eccentricity in our simulations to be $\lesssim 0.01$, and we find that it decreases with increasing resolution, with only a mild dependence on coupling. This suggests that residual eccentricity from the initial data is subdominant to finite-resolution numerical errors, and does not significantly affect the dephasing of the binary. The eccentricity of the binary system is not much affected by the value of the Gauss-Bonnet coupling, as even for the

largest couplings we consider the energy contained in the scalar cloud is only a small fraction of the total binary binding energy, and an even smaller fraction of that energy is radiated away during the scalarization process.

C. Merger dynamics

Lastly, we mention the effects of ESGB on the merger dynamics of equal mass binaries with couplings $\zeta_1 = 0.01$ and 0.05, compared to GR. Figure 7 shows the gravitational wave emission starting slightly before merger, and including the ringdown, for different values of ζ_1. We find that while the ESGB waveforms have a noticeable dephasing relative to GR, consistent with the fact that ESGB binaries should merge faster due to the additional energy loss through scalar radiation, the peak amplitude of the gravitational wave at merger depends only very weakly on ζ_1. The effect of modified gravity on the frequency and decay rate of the quasinormal modes is also too small to reliably quantify with our current numerical data, so we defer a more detailed study of the ringdown to future work.

In the right panel of Fig. 7 we show the leading $\ell = m = 2$ mode of the scalar waveform after rescaling for the test-field dependence on the coupling, which implies that the amplitude of ϕ scales linearly with ζ_1. For the $\zeta_1 = 0.05$ case, we find an additional nonlinear enhancement in the scalar field amplitude at merger, with $|\phi|/\lambda$ roughly 5% higher compared to the $\zeta_1 = 0.01$ case.

The negligible effect on the GW amplitude with varying ESGB coupling that we find here contrasts with the large effect found in order-reduced simulations. In particular, the correction to Ψ_4, which scales quadratically with ζ_1 in the perturbative approach taken in Ref. [19], gives an order-one correction to the amplitude for the highest couplings used here (see Fig. 2 of Ref. [19]); though we note that Ref. [19] also uses a slightly different mass-ratio ($q = 0.82$) and
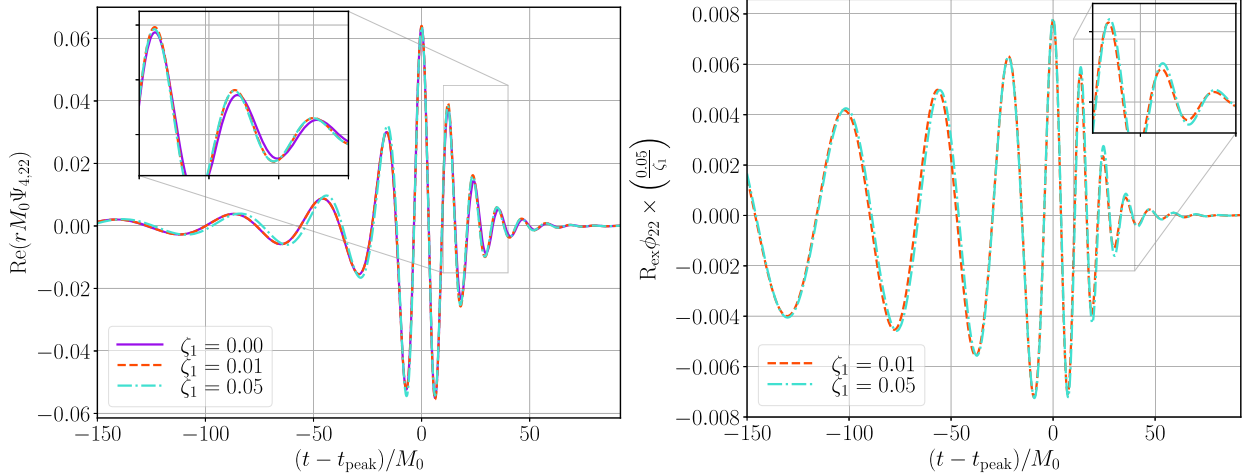
FIG. 7. Gravitational wave radiation (left) and scalar radiation (right) for equal mass ratio binaries with coupling $\zeta_1 = 0$, 0.01, and 0.05. We show the real part of the $\ell = m = 2$ spherical harmonics of the Newman-Penrose scalar Ψ_4 and ϕ. Time is measured with respect to the time where the complex amplitude of $\Psi_{4,22}/\phi_{22}$ peaks. We add an overall phase so that the waveforms are real and positive at $t = t_{\text{peak}}$.

nonzero spins for the constituent black holes. We speculate that this qualitative difference behavior in the waveform is due to the presence of secularly growing errors terms, which are known to be present in such a perturbative approach to evolving modifications to GR. For more discussion of this phenomena, see Refs. [18,19,70].

V. DISCUSSION AND CONCLUSION

In this work, we have performed the first systematic study of the nonlinear dynamics of binary black hole inspiral and merger in sGB gravity. We considered several values of the sGB coupling and the binary mass ratio, and compared our results to PN theory. Solving the full equations of motion allowed us to directly measure the increased dephasing of the inspiral due to the emission of scalar radiation, and to determine the relative effects of nonlinearity on the scalar and gravitational waveforms. We argue that, at least in the last few orbits of the inspiral phase before merger, PN theory is currently not accurate enough to determine the dephasing of the binary due to the modified gravity, even taken as a correction to a more accurate to GR waveform.

In addition to measuring the dephasing of binary black holes, we find that leading-order PN theory (in the GB coupling λ) does well in matching the amplitude of scalar radiation emitted during the inspiral phase, given the frequency of observed gravitational radiation. This is in general qualitative agreement with earlier numerical relativity work that compared simulations of sGB gravity in the decoupling limit to PN predictions [38]. The success of leading order PN theory in matching the scalar waveform can be partially explained by the fact that corrections to the scalar field amplitude in the GB coupling enter at order ζ_1^3 for sGB gravity (see Appendix D).

We have studied the dynamics of the merger for a limited number of cases, where we found that when the black holes merge the effect due to the ESGB modifications on the peak amplitude of the gravitational wave signal is small, in contrast to what results using perturbative treatments of the merger would suggest. We leave a detailed study of the detectability of these effects and their degeneracy with different intrinsic parameters to future work.

In this first study, for computational expediency, and given that the ESGB equations of motion are more complicated to solve than the GR ones, we have focused on the roughly last 8 orbits before merger. However, an obvious direction for future work is to consider binaries that start at wider separations (and hence lower orbital and gravitational wave frequencies), in order to determine at what point leading-order PN theory becomes accurate. Modeling the merger is arguably the most important contribution numerical relativity can make to our understanding of binary black hole evolution. As we were unable to evolve through merger for larger coupling values understanding this limitation of our code/methods remains an important task for future work. Different choices of gauge or auxiliary metrics, as well developing better diagnostics for monitoring the breakdown of hyperbolicity may help address this. As mentioned above, we believe one of the main difficulties lie in being able to excise elliptic regions near merger, around the time the final remnant black hole forms from the merger. Our algorithm may be improved by implementing a more complicated excision surface (currently we only excise an ellipsoidal region), and working with higher resolution, to more stably excise closer to the surface of the apparent horizons. We note that recent work [43] reports evolutions of nonspinning, equal mass ratio black hole binaries through merger using a modified

CCZ4 formulation of the equations of motion with puncturelike coordinates, for ζ_1 values as large as $\zeta_1 = 0.1/\sqrt{2} \sim 0.07$ (converting to our conventions). In that work, the authors make use of an effective excision algorithm by letting the modified gravity coupling go to zero at small values of the spatial metric conformal factor, as in Refs. [71,72]; such a method may be useful in conjunction with our direct excision method to stabilize the evolution near the excision boundary.

In this work, we only considered binary black hole systems where the individual black holes were initially nonspinning. As black hole spin can significantly impact the dynamics of binaries in GR, a natural next step to this work would be to consider black hole spin. Furthermore, introducing spin may lead to novel gravitational wave signatures as, for example, in black hole spin-induced spontaneous scalarization [73–75].

We have only simulated the dynamics of arguably the simplest of the ESGB gravity theories that gives scalar hairy black holes. Other kinds of scalar Gauss-Bonnet couplings [i.e., more general terms of the form $\beta(\phi)\mathcal{G}$ in the action] can allow for a rich range of phenomena, most notably the effect of spontaneous (de)scalarization, which so far has only been studied either perturbatively [39,76], or in symmetry-reduced settings [73–75,77–81]. As well, including a term of the form $f(\phi)X^2$ in the action is also "natural" from an effective-field theoretic point of view, as this is another four derivative term that is also parity-invariant [41,82], and may have some effect on the binary evolution. Simulating nonlinear effects such as spontaneous black hole scalarization requires understanding the backreaction of the scalar field on the background geometry, as that affects the saturation of the instability and end state black hole, and determines which effects occur in the regime where the theory remains hyperbolic [81]. Accurately simulating theories with high precision that exhibit spontaneous black hole scalarization will additionally require the development of initial data solvers that solve the constraint equations in sGB gravity that have an initially nontrivial scalar field profile [23,83]. It would also be interesting to extend recent work on binary neutron star mergers [40] to study black hole–neutron star binaries in ESGB gravity (earlier work on spontaneous scalarization in ESGB gravity for single neutron star solutions include Ref. [84]).

The particular version of the initial data code we use can be accessed at Standalone TwoPunctures.[3]

APPENDIX A: CONVERGENCE TESTS AND ACCURACY OF OUR SIMULATIONS

Here we quantify the main sources of error in our simulations, which include the numerical truncation error, finite radius extraction effects, and residual orbital eccentricity.

1. Truncation error and convergence

We first consider the truncation error, which is due to the finite resolution of the simulations. The simulations of the binary black hole systems with mass ratio $q = 1$ and $q = 2/3$ presented in this work use eight levels of adaptive mesh refinement with a refinement ratio of $2:1$, and have a linear grid spacing of $dx = 0.012M_0$ on the finest level containing the smallest back hole. The results for the mass ratio $q = 1/2$ use nine levels of adaptive mesh refinement and a grid spacing of $dx = 0.006M_0$ around the smallest black hole. In Fig. 8, we plot the integrated constraint violation for a $q = 2/3$, $\zeta_1 = 0.075$ binary with grid spacing that is $4/3$ and $\times 2/3$ as large as default resolution. We also perform a resolution study of a $q = 1/2$, $\zeta_1 = 0.075$ binary, where the linear spacing of the medium resolution is $dx = 0.005M_0$ and covers the smallest black hole. The integrated constraints shown in Fig. 8 have grid spacing $4/3$ and $\times 2/3$ as large as medium resolution. We see roughly third-order convergence in the constraint violation. Though we use fourth-order finite difference
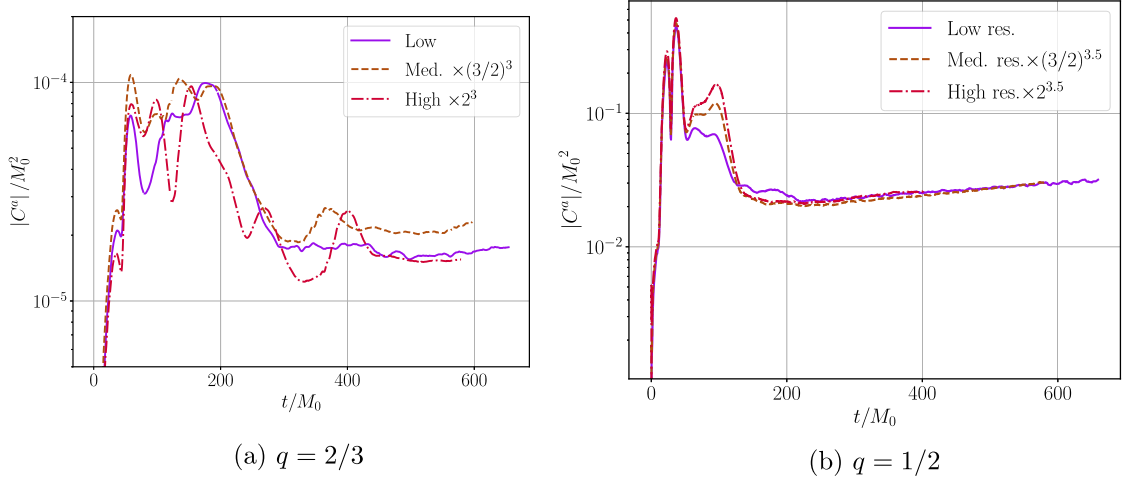

(a) $q = 2/3$

(b) $q = 1/2$

FIG. 8. Volume integrated norm of the constraint violation as a function of time for a nonspinning $q = 2/3$ and $q = 1/2$ binary black hole merger with $\zeta_1 = 0.075$ at three resolutions. The medium and high resolutions have $1.5\times$ and $2\times$ the resolution of the low resolution on the coarsest grid. We observe roughly third-order convergence of our runs, which is consistent with the third order in time interpolation used on the boundaries of adaptive mesh refinement grids [52,88].

(a) Amplitude A of ϕ_{11}, $q = 1/2$

(b) Amplitude A of $\Psi_{4,22}$, $q = 1/2$

(c) Phase Φ of ϕ_{11}, $q = 1/2$

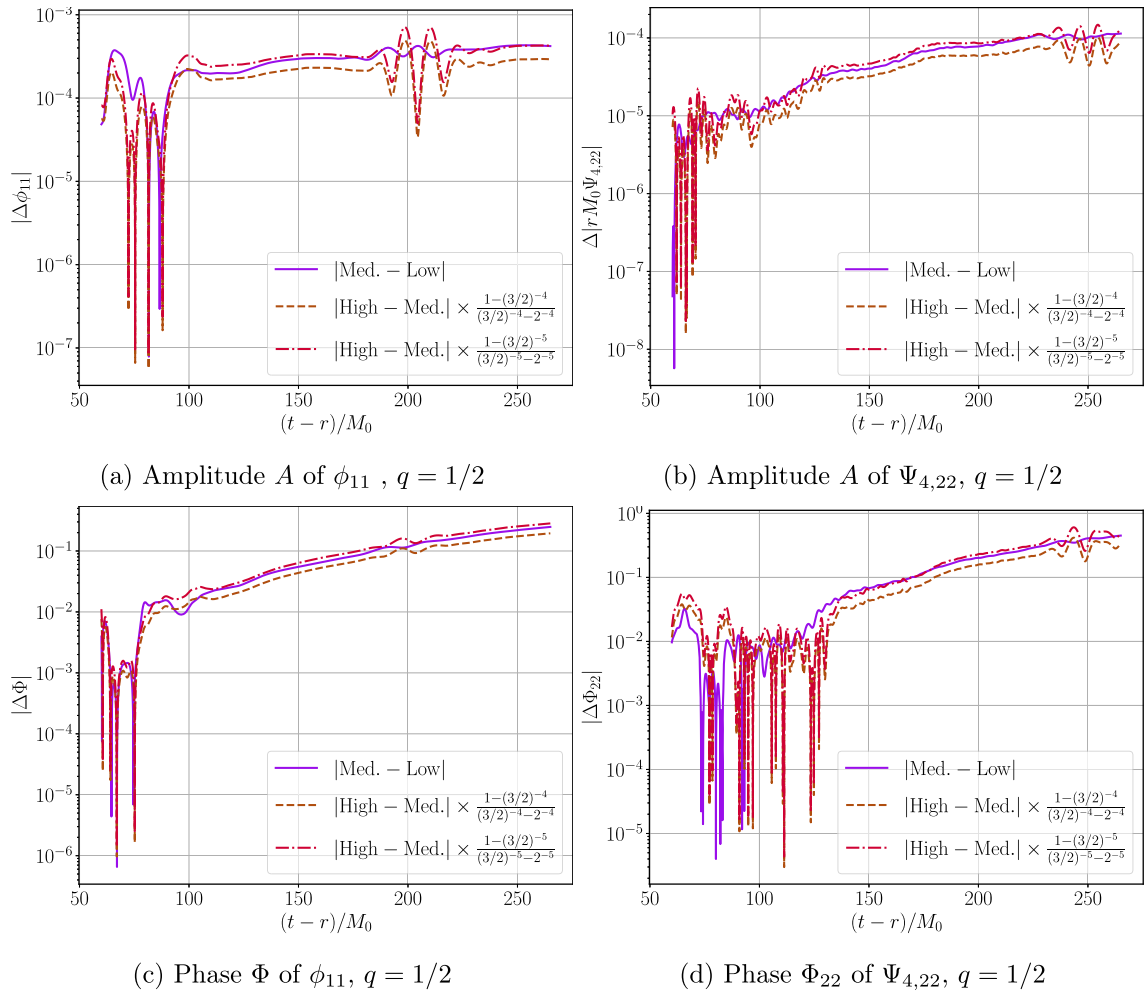(d) Phase Φ_{22} of $\Psi_{4,22}$, $q = 1/2$

FIG. 9. We show the absolute differences between the low, medium, and high resolutions of the amplitude and phase of the scalar (left) and tensor (right) waveforms for a nonspinning BH binary with mass ratios $q = 1/2$ and coupling $\zeta_1 = 0.075$. We see that the waveform converges at between fourth order and fifth order (corresponding to the scaling used for the dashed and the dashed-dotted lines, respectively). Note that we only show the scalar waveform from $50M$ onwards as the scalar field is zero before then.

(a) Phase Φ of ϕ_{11}

(b) Phase Φ_{22} of $\Psi_{4,22}$

(c) Amplitude A of ϕ_{11}

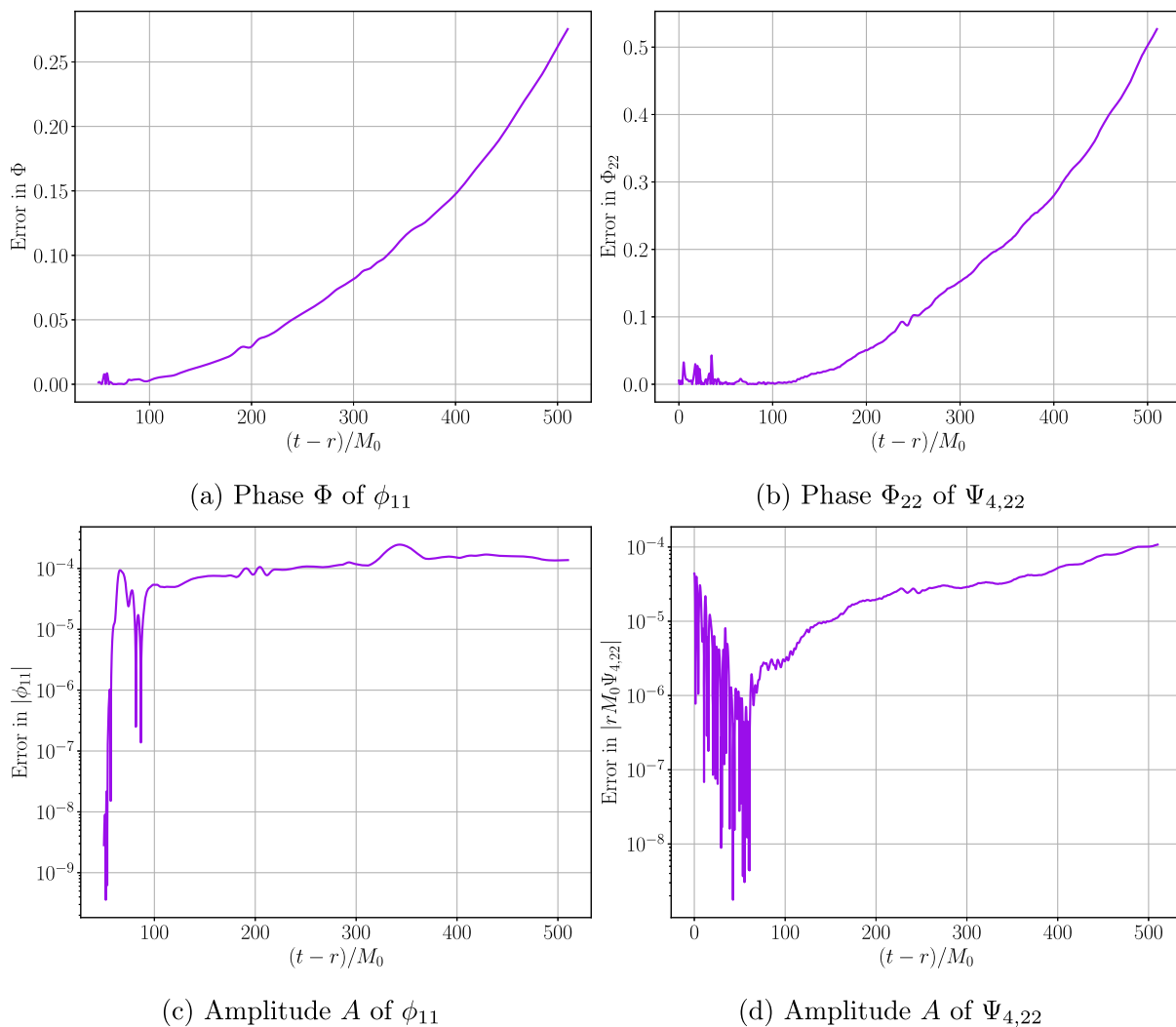

(d) Amplitude A of $\Psi_{4,22}$

FIG. 10. Truncation error estimate of the medium resolution obtained from the Richardson extrapolation of the phase $\Phi(t)$ and amplitude $A(t)$ of the scalar (left) and tensor (right) waveform extracted at $100M_0$ for a nonspinning BH binary with mass ratio $q = 1/2$ and coupling $\zeta_1 = 0.075$.

stencils and Runge-Kutta time integration, this level of convergence is consistent with the third-order interpolation in time used to set values on the boundaries of adaptive mesh refinement levels.

In Fig. 9, we plot the self-convergence of the amplitude and phase for $\Psi_{4,22}$ and ϕ_{11} for the $q = 1/2$, $\zeta_1 = 0.075$ run. Unlike the integrated constraint violation, we find that $\Psi_{4,22}$ and ϕ_{11} converge at roughly fourth order for $q = 1/2$. For the same run, we show the Richardson extrapolated error in the phase and amplitude for $\Psi_{4,22}$ and ϕ_{11} (Fig. 10).

As discussed in Sec. IV, because we use the same numerical resolution for carrying out the GR and sGB simulations, which we then compare to compute the dephasing $\delta\Phi$, there is a cancellation which leads to a smaller truncation error in this quantity compared to the overall truncation error in Φ. This is illustrated in Fig. 11,

where we estimate the truncation error in $\delta\Phi$ by comparing a $q = 1/2$ GR simulation to an equivalent sGB simulation with $\zeta_1 = 0.075$ at two different resolutions. We compare this to an estimate of the overall truncation error in Φ for the same sGB case, and carry out a similar comparison for the GW amplitude.

2. Extraction error of waveforms

We next consider the extraction error, that is, the errors in our waveforms due to extracting them at a finite radius. To estimate the extraction error we compute the complex amplitude and phase of the $(\ell = 2, m = 2)$ multipole of Ψ_4 defined in Eq. (A3) and the $(\ell = 1, m = 1)$ multipole of ϕ defined in Eq. (5b) at several extraction radii, and extrapolate the quantities to infinity by fitting them to polynomials in $1/r$

(a) Amplitude A of $\Psi_{4,22}$, $q = 1/2$

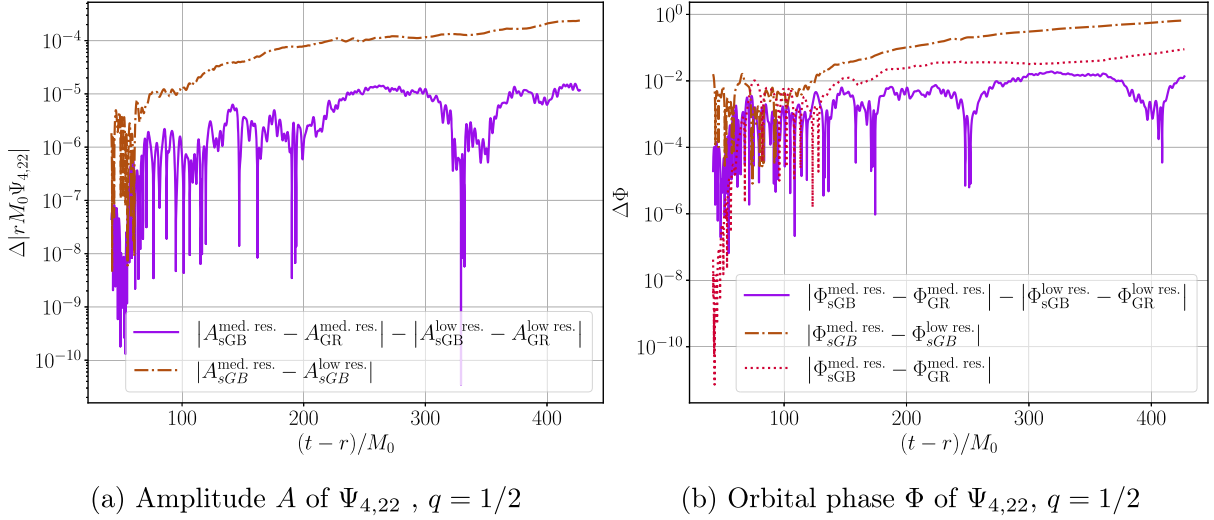(b) Orbital phase Φ of $\Psi_{4,22}$, $q = 1/2$

FIG. 11. We show the difference between the low and medium resolutions of the amplitude (left) and phase (right) of the gravitational waveform for a nonspinning BH binary with mass ratio $q = 1/2$ and coupling $\zeta_1 = 0.075$ (solid purple) and the difference of the difference between the sGB and GR amplitude and phase at low and medium resolutions (dashed-brown line). This provides evidence that the truncation error roughly cancels between the sGB and GR runs.

$$A(r, t_{\rm ret}) = \sum_{n=0}^{N} \frac{A^{(n,N)}(t_{\rm ret})}{r^n}, \qquad (A1a)$$

$$\chi(r, t_{\rm ret}) = \sum_{n=0}^{N} \frac{\chi^{(n,N)}(t_{\rm ret})}{r^n}. \qquad (A1b)$$

where $t_{\rm ret} = t - r$ refers to the retarded time, A is the amplitude of the waveform, and χ is the phase. The time-dependent $n = 0$ coefficients are then used as the amplitude and phase of the asymptotic waveform. The error from computing a field quantity $u(t_{\rm ret}, r)$ at a finite radius r_i is then

$$\epsilon(u, r_i, N) = |u(t_{\rm ret}, r_i) - u^{(0,N)}(t_{\rm ret})|. \qquad (A2)$$

In Figs. 12 and 13, we plot our estimates for the error due to the extraction of the gravitational and scalar waveforms at a finite radius. Comparing these to the estimate of the truncation error in Fig. 10 we conclude that the finite resolution of the code is the dominant source of error.

3. Orbital eccentricity

To estimate the orbital eccentricity of the binary system, introduced by imperfect initial data, we use the

(a) Phase Φ_{22}

(b) Amplitude A

FIG. 12. Deviation of the phase, $\epsilon(\Phi_{22}, r_i, 1)$ (left) and relative deviation of the amplitude, $\epsilon(A, r_i, 1)/A_{0,1}$ (right) of the waveform $r\Psi_{4,22}(t, r)M_0 = A(t, r)e^{i\Phi_{22}(t,r)}$ obtained at finite extraction radius from the values extrapolated according to Eq. (A1) for a nonspinning BH binary with mass ratio $q = 1/2$ and coupling $\zeta_1 = 0.075$.
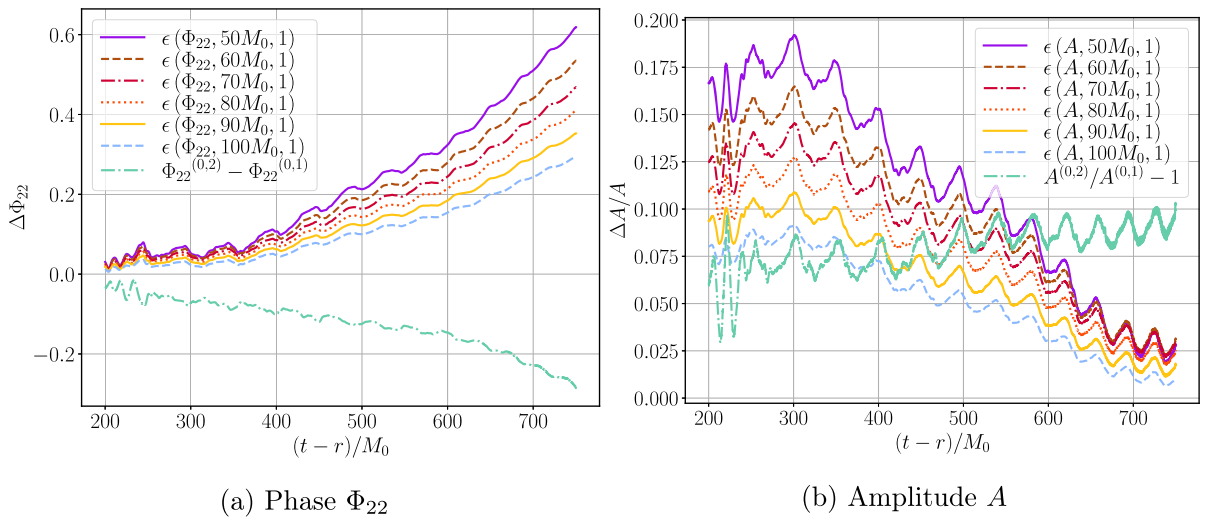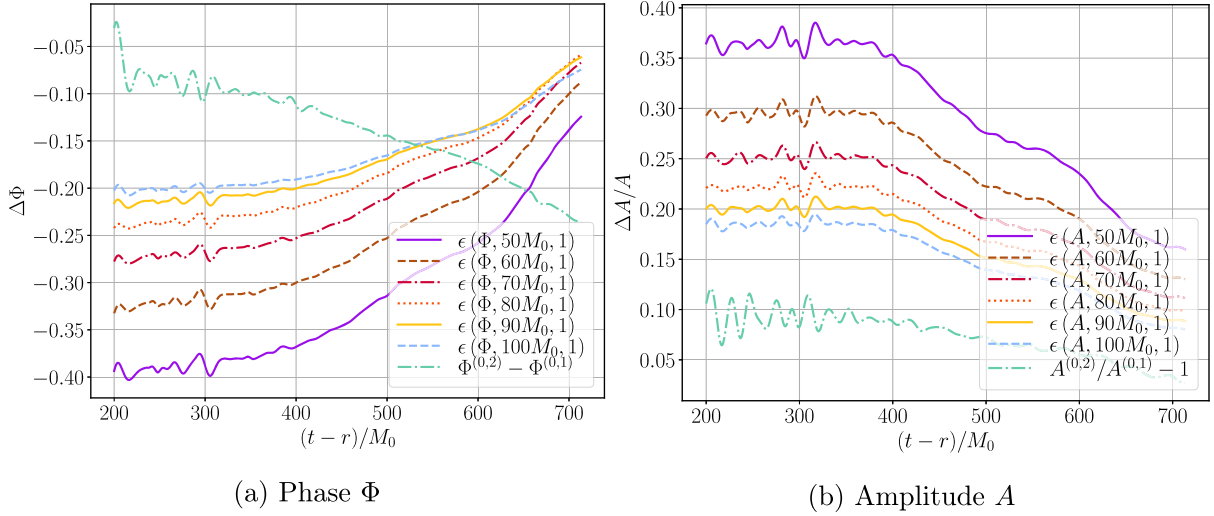
(a) Phase Φ (b) Amplitude A

FIG. 13. Deviation of the phase, $\epsilon(\Phi, r_i, 1)$ (left) and relative deviation of the amplitude, $\epsilon(A, r_i, 1)/A_{0,1}$ (right) of the waveform $(r/M_0)\phi_{11}(t, r) = A(t, r)e^{i\Phi(r,t)}$ obtained at finite extraction radius from the values extrapolated according to Eq. (A1) for a nonspinning BH binary with mass ratio $q = 1/2$ and coupling $\zeta_1 = 0.075$.

gravitational wave phase [89]. We write the $(\ell, m) = (2, 2)$ component of Ψ_4 in the wave zone as

$$rM_0 \times \Psi_{4,22} \equiv A_{22}(t, r)e^{-i\Phi_{22}} + \mathcal{O}\left(\frac{1}{r}\right). \qquad \text{(A3)}$$

We fit a fifth-order polynomial to the orbit-averaged Φ to obtain Φ_{fit}, and define the eccentricity to be the amplitude of the oscillating function

$$e_\Phi(t) \equiv \frac{\Phi_{22}(t) - \Phi_{\text{fit},22}(t)}{4}. \qquad \text{(A4)}$$

We plot the eccentricity [see Eq. (A4)] of our simulations in Fig. 14 for different values of ζ_1 and resolution. Ideally, an eccentricity estimator will plot a sinusoidal wave as a function of time [89]. Our eccentricity measurements have higher harmonics, which we attribute to the junk radiation from the choice of puncture initial data, and from the black hole scalarization process, and from the fact that we only measure the eccentricity over a relatively short inspiral time ($t/M_0 < 1000$). While the eccentricity does slightly increase with increasing ζ_1, we find that our eccentricity is mostly limited by resolution, and not from perturbations caused by our initial data. This suggests that the dephasing between the sGB and GR simulations is not dominated by small differences in the eccentricity of our simulations caused by the rapid development of the scalar field around the black holes at early times.

APPENDIX B: POST-NEWTONIAN RESULTS IN SGB GRAVITY

Due to the presence of monopole scalar charge around each black hole in sGB gravity, black hole inspirals can emit scalar radiation, which enters at -1PN order as dipole emission for unequal mass black hole binaries. The calculation of the leading PN correction to the gravitational and scalar radiation for binary black holes in sGB gravity was carried out in Ref. [34]. In the limit of an exactly equal mass, nonspinning binary, the dipole radiation vanishes. More generally it is straightforward to see that any odd multipole of a scalar is zero in this case as the spherical harmonics are odd under parity inversion ($\vec{r} \to -\vec{r}$), but the spacetime in this case is even under this transformation. Thus, for equal mass black hole binaries, the scalar waveform enters at higher PN order [34,36,37].

The PN calculations initiated in Ref. [34] were recently extended to higher PN order in Refs. [36,37]. In those works, the authors additionally considered more general Gauss-Bonnet couplings $f(\phi)\mathcal{G}$. Here we only present the leading-order PN results. To leading order in ζ_1, spherical harmonic components of the scalar radiation of the binary system go as [34,36–38])

$$\phi_{00} \approx \left(\frac{2\lambda}{r}\right)(8\pi)^{1/2}\frac{M_0}{m_1 m_2}, \qquad \text{(B1a)}$$

$$\phi_{11} \approx -\left(\frac{2\lambda}{r}\right)\left(\frac{2\pi}{3}\right)^{1/2}\left(1 + \frac{3m_1^2 + 3m_2^2 + 4m_1 m_2}{M_0^2}x\right) \\ \times \frac{\Delta M_0}{m_1 m_2}x^{1/2}, \qquad \text{(B1b)}$$

$$\phi_{22} \approx -\left(\frac{2\lambda}{r}\right)\left(\frac{8\pi}{15}\right)^{1/2}\frac{m_1^2 - m_1 m_2 + m_2^2}{M_0 m_1 m_2}x, \qquad \text{(B1c)}$$

$$\phi_{33} \approx \left(\frac{2\lambda}{r}\right)\left(\frac{1296\pi}{35}\right)^{1/2}\frac{\Delta M(m_1^2 + m_2^2)}{8M_0^2 m_1 m_2}x^{3/2}, \qquad \text{(B1d)}$$
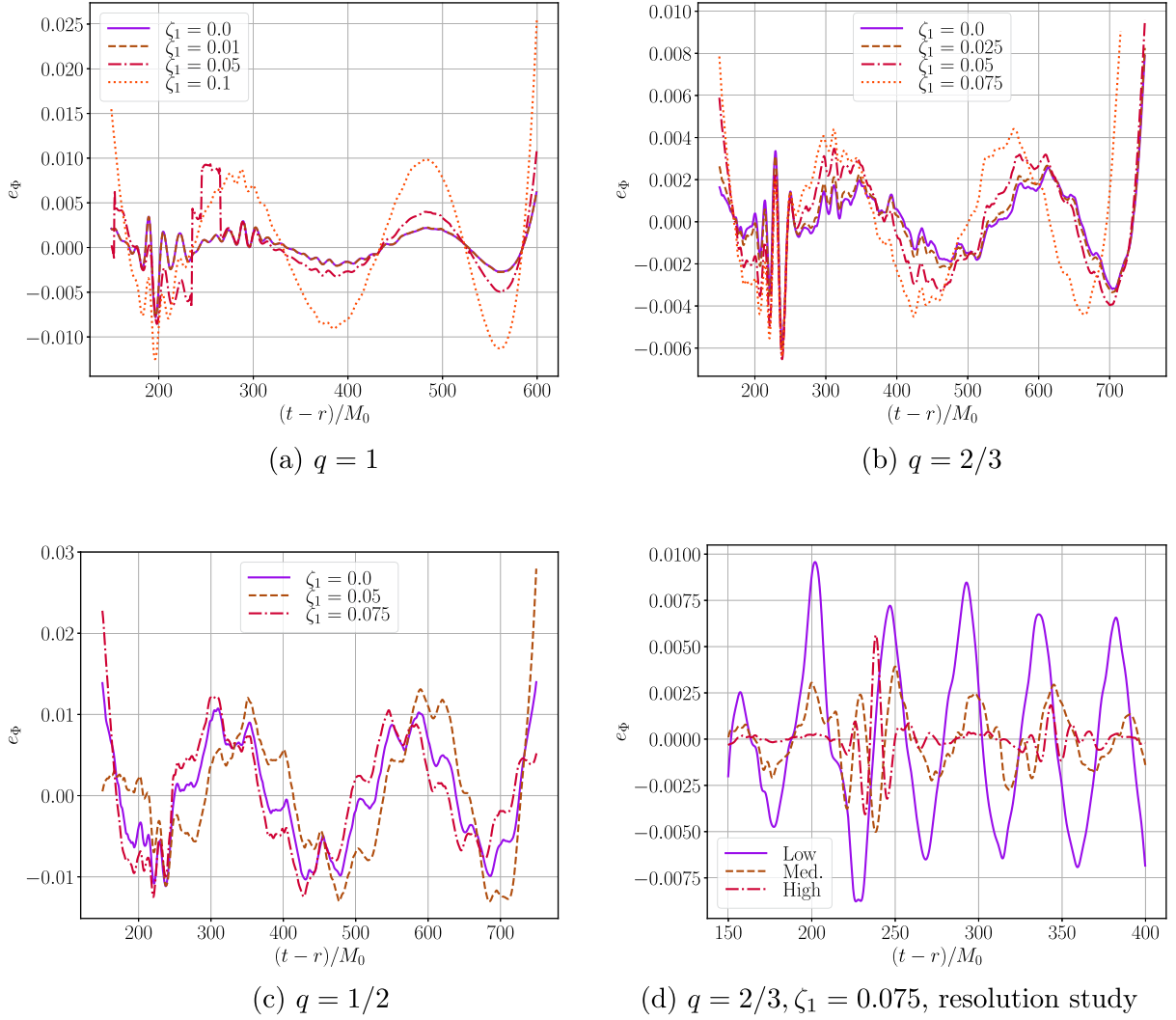
(a) $q = 1$

(b) $q = 2/3$

(c) $q = 1/2$

(d) $q = 2/3, \zeta_1 = 0.075$, resolution study

FIG. 14. Eccentricity estimator of the $q = 1$, $q = 2/3$, and $q = 1/2$ mass ratio inspirals for several different values of ζ_1, and for the $q = 2/3$ mass ratio at different resolutions. We see that the eccentricity of the binaries we study is affected by both the form of our initial data (the formation of scalar charge from vacuum initial conditions), and, to a greater extent, from the resolution of our runs. We measure the eccentricity using the radially extrapolated Weyl scalar $\Psi_{4,22}$. The low and high resolution have $2/3$ and $4/3\times$ the resolution of the medium resolution which has a linear grid spacing of $dx = 0.006M_0$ on finest level.

$$\phi_{44} \approx \left(\frac{2\lambda}{r}\right)\left(\frac{2048\pi}{315}\right)^{1/2}$$
$$\times \frac{m_1^4 - m_1^3 m_2 + m_1^2 m_2^2 - m_1 m_2^3 + m_2^4}{3m_1 m_2 M_0^3} x^2, \quad \text{(B1e)}$$

where $m_{1,2}$ are the masses of the two black holes, with the convention $m_1 \leq m_2$ (see Sec. III B), Ω is the angular velocity of the binary in the center of mass frame, and

$$\phi_{\ell m} \equiv \lim_{r \to \infty} \int_{\mathbb{S}_2} \bar{Y}_{lm}\phi, \quad \text{(B2a)}$$

$$M_0 \equiv m_1 + m_2, \quad \text{(B2b)}$$

$$\Delta M \equiv m_2 - m_1, \quad \text{(B2c)}$$

$$x \equiv (M_0\Omega)^{2/3}. \quad \text{(B2d)}$$

Note that the second terms in Eq. (B1), which are raised to the $1/2$ power, come from the integral over the sphere of $\bar{Y}_{lm}$. The scalar waveforms Eq. (B1) are presented to leading order in the PN expansion, except for the $\ell = m = 1$ waveform, which has been computed to 0.5PN order [36,37].

We next consider the dephasing of gravitational waves in PN theory. We write the orbital phase in the time domain as a function of the PN parameter x,

$$\Phi(x) = \Phi_{\text{GR}}(x) + \delta\Phi(x). \quad \text{(B3)}$$

Here, Φ_{GR} is the orbital phase when setting $\lambda = 0$, and $\delta\Phi$ is the additional phase shift that comes from the emission of

scalar radiation. In the PN expansion of scalarized compact objects, there are two limits considered in the literature; the *dipole driven regime* and the *quadrupole driven regime* [35,37]. In the dipole driven regime, the dipole scalar emission is the dominant source of radiated energy, while in the quadrupole driven regime, the dominant source of radiated energy is the gravitational wave emission. The system is in the quadrupole driven regime when

$$x \gtrsim \frac{5}{24} \mathcal{S}_-^2, \tag{B4}$$

where we introduced the scalar dipole

$$\mathcal{S}_\pm \equiv \frac{\alpha_2 \pm \alpha_1}{2\sqrt{\bar{\alpha}}}, \tag{B5}$$

where $\bar{\alpha} \equiv (1 + \alpha_1 \alpha_2)$, and α_i are the *black hole sensitivities* for sGB gravity [45,46] [for their explicit values, see Eq. (B6) below]. Notice, for equal mass ratio binaries, the system is always in the quadrupole driven regime as there is no dipole radiation ($\mathcal{S}_- = 0$). We see that the system is in the dipole driven regime only for unequal mass ratio binaries that are far apart (that is, when x is small). Given the experimental constraints on $\zeta_1 \ll 1$ and $\mathcal{S}_-$, the binary systems of interest for ground- and space-based GW detectors are driven by the quadrupolar driven regime for sGB gravity. We thus compare our numerical waveforms to gravitational waveforms for systems in which quadrupolar radiation is dominant.

The leading-order contribution to the GW phase in ESGB gravity was computed in Refs. [34,90] using the stationary-phase approximation [61], and later extended to higher orders in PN theory in Refs. [36,37,51]. The highest-order PN corrections to the phase so far have been computed by Lyu *et al.* [51], who mapped results obtained partially to 2PN order in scalar-tensor theories [35] to sGB gravity. Here, we review their calculation, and present results for the time-domain orbital phase $\delta\Phi$ as a function of the PN parameter x.

The results of Ref. [35] were presented in the Jordan frame, and ESGB gravity is written in the Einstein frame. Thus, the first step Lyu *et al.* took was to transform the results of Ref. [35] to the Einstein frame. After this transformation, Lyu *et al.* noticed that the results of Ref. [35] were expressed in terms of the black hole sensitivities α_i, and their derivatives β_i. These were computed for black holes in ESGB gravity by Julié *et al.* [45,46], and for nonspinning black holes are given by (here we used the conversion $\varphi \to \phi/\sqrt{2}$, $f(\varphi) \to 2\sqrt{16\pi}\varphi$, and $\alpha_{GB} \to \lambda/\sqrt{8\pi}$)

$$\alpha_i \equiv -\frac{\alpha_{GB}f'(\varphi_0)}{2m_i^2} = -\frac{\sqrt{2}\lambda}{m_i^2}, \tag{B6}$$

$$\beta_i \equiv \frac{d\alpha_i}{d\varphi}\bigg|_{\varphi_0} = -\frac{\alpha_{GB}^2 f'(\varphi_0)^2}{2m_i^2} = -\frac{4\lambda^2}{m_i^2}, \tag{B7}$$

where φ_0 is the asymptotic value of scalar field at infinity (we set $\varphi_0 = 0$). We see that $\beta_i \propto \lambda^2$, so it is negligible compared to α_i. Using these expressions, and keeping terms up to $\mathcal{O}(\lambda^2)$, sGB corrections to the orbital phase in the quadrupolar driven regime can be expressed as

$$\delta\Phi(x) = \sum_i \delta\Phi_{i,PN} = \frac{\lambda^2}{8\pi m_1^4 m_2^4 \eta} \sum_i c_i x^{(-5+2i)/2}, \tag{B8}$$

where

$$c_{-1} = \frac{25\pi}{1344}(m_2^2 - m_1^2)^2 \tag{B9}$$

$$c_0 = \frac{5\pi}{32256}[(659 + 728\eta)(m_2^2 - m_1^2)^2] + \frac{5\pi}{12}m_2^2 m_1^2 \tag{B10}$$

$$c_{0.5} = -\frac{25\pi}{384}(m_2^2 - m_1^2)^2(3\pi + f_3^{ST}) \tag{B11}$$

$$\begin{aligned}
c_1 &= \frac{5\pi}{585252864}[55883520(m_2^3 m_1 + m_2 m_1^3) \\
&\quad + 25(1640783 + 2621304\eta + 2095632\eta^2)(m_2^4 + m_1^4) \\
&\quad - 2m_1^2 m_2^2(83960375 + 43179192\eta + 52390800\eta^2)] \\
&\quad - \frac{25\pi}{288}(m_2^2 - m_1^2)^2 f_4^{ST}
\end{aligned} \tag{B12}$$

$$\begin{aligned}
c_{1.5} &= -\frac{5\pi^2}{12}(m_2^4 - 14m_1^2 m_2^2 + m_1^4) \\
&\quad - \frac{5\pi}{96}(m_2^4 - 6m_1^2 m_2^2 + m_1^4)f_3^{ST} + \frac{1}{\lambda^2}\frac{5\pi}{8}m_1^4 m_2^4 f_3^{ST}
\end{aligned} \tag{B13}$$

$$\begin{aligned}
c_2 &= \frac{5\pi}{48771072}[-24385536(m_2^3 m_1 + m_2 m_1^3) \\
&\quad + (4341025 - 65553264\eta + 684432\eta^2)(m_1^4 + m_2^4) \\
&\quad + 54m_1^2 m_2^2(-12500965 + 19310256\eta + 366128\eta^2)]
\end{aligned} \tag{B14}$$

$$-\frac{5\pi}{48}(m_2^4 - 14m_1^2 m_2^2 + m_1^4)f_4^{ST} + \frac{1}{\lambda^2}\frac{5\pi}{4}m_1^4 m_2^4 f_4^{ST}, \tag{B15}$$

and $\eta \equiv m_1 m_2/M_0^2$ is the symmetric mass ratio. Our calculation of these coefficients are presented in an ancillary Mathematica notebook [91]. As noted in Ref. [51], the leading -1PN term here agrees with the one found in Refs. [34,90]. We note that we have *not* included black hole spin dependence here (in the notation of Ref. [51], we have set $s_i = 1$, although the notebook presents results for general s_i). The terms at 0.5PN onwards contain currently unknown coefficients f_{2n}^{ST}, which represent our ignorance of the new scalar contributions at relative $n = 1.5$ and $n = 2$PN order in the nondipolar flux (part of the flux that does not

vanish for an equal mass binary) beyond 1PN order [35]; we see that f_{2n}^{ST} must scale as λ^{2+n}, $n > 0$ in order for these terms to not be important as $\lambda \to 0$. In the quadrupolar-driven regime, experimental constraints on the weak-field parameters of scalar-tensor gravity suggest that these contributions should be much smaller than the 2PN GR terms [35], so f_{2n}^{ST} is set to zero in Ref. [51] and in this work.

APPENDIX C: PUNCTURE INITIAL DATA FOR SGB BINARY BLACK HOLE EVOLUTION

As we discuss in Sec. III B, the Hamiltonian and momentum constraint equations in sGB gravity reduce to those of GR when $\phi = \partial_t \phi = 0$ on the initial data hypersurface [22,23], and we make use of GR puncture initial data in our simulations. While puncture initial data is well known [92] and the TwoPunctures implementation of that formalism is widely used [54], to our knowledge it has never been implemented in conjunction with black hole excision and a (modified) generalized harmonic formulation. Here, we review puncture initial data, and how we incorporated the TwoPunctures initial data in our MGH code.

First we write the metric in ADM variables,

$$ds^2 = -N^2 dt^2 + h_{\alpha\beta}(dx^\alpha + N^\alpha dt)(dx^\beta + N^\beta dt). \quad \text{(C1)}$$

The extrinsic curvature is

$$K_{\alpha\beta} = -\frac{1}{2N}(\partial_t h_{\alpha\beta} - D_\alpha N_\beta - D_\beta N_\alpha), \quad \text{(C2)}$$

where D_α is the extrinsic curvature with respect to the spatial slice.

Puncture initial data is spatially conformally flat and maximally sliced ($K = 0$), and sets $h_{\alpha\beta} = \psi^4 \delta_{\alpha\beta}$, that is the initial spatial metric is conformally flat. The extrinsic curvature is specified by choosing a set of effective black hole masses $m_{(n)}$, spins $S_{(n)}^\gamma$, momenta $P_{(n)}^\gamma$, and locations. One then solves the Hamiltonian constraint for ψ, which then gives us $h_{\alpha\beta}$ (the momentum constraint is solved using an analytic formula). Puncture initial data does not specify the lapse N and shift N^γ. We set $N^\alpha = 0$, and choose N to be (we set the initial-lapse parameter to twopunctures-averaged in the TwoPunctures code [54])

$$N = \left(1 + \frac{m_1}{2r_1} + \frac{m_2}{2r_2}\right)^{-1}, \quad \text{(C3)}$$

where r_i is the radial (Euclidean) distance from the ith puncture. To recover the metric initial data from the ADM variables, we invert the definitions to get

$$g_{tt} = -N^2, \qquad g_{t\alpha} = 0,$$
$$g_{\alpha\beta} = h_{\alpha\beta}, \qquad \partial_t g_{tt} = -2N\partial_t N,$$
$$\partial_t g_{t\alpha} = 0, \qquad \partial_t g_{\alpha\beta} = -2NK_{\alpha\beta}. \quad \text{(C4)}$$

In puncture coordinates, the black hole apparent horizon is located at $r = m/2$. We then initially excise an ellipsoid inside that surface on our $t = 0$ slice after the TwoPunctures code has solved for the conformal factor and interpolated the result on the initial Cartesian grid we use. The MGH parameters $\hat{g}^{ab}$, $\tilde{g}^{ab}$, and H_a determine $\partial_t N$ and $\partial_t N_\alpha$.

We set $S_{(1,2)}^\gamma = 0$, so that the black holes are initially nonspinning. We choose quasicircular initial data for the momenta $P_{(1,2)}^\gamma$. In particular, given r and $m_{(n)}$, we set (here using spherical polar coordinates)

$$P_{(n)}^\gamma \partial_\gamma = m_{(n)} \times (\dot{r}\partial_r + r\Omega\partial_\phi). \quad \text{(C5)}$$

We choose $\dot{r}$ to be accurate to 2.5PN order for a quasicircular binary, that is it incorporates the leading-order radiation reaction term, and we choose Ω to be accurate to 2 PN order for a quasicircular binary [56,93,94].

We note that Kovacs [83] has recently constructed a more general set of puncture initial data for black holes in sGB gravity, which reduces to the original puncture data for GR that we use here when one chooses the initial values of $\phi = \partial_t \phi = 0$.

APPENDIX D: PERTURBATIVE SOLUTIONS TO SGB GRAVITY

Here, we briefly review the perturbative approach to solving the equations of motion in shift-symmetric ESGB (sGB) gravity. While we do not employ the perturbative method in this work (instead, we solve the full sGB equations of motion), all previous numerical relativity work comparing to PN theory has [36–38]. As in those earlier results, we find that at a given frequency, the amplitude of our scalar waveforms are very similar to the scalar waveforms produced in the decoupling limit; however, here we are able to directly measure the extra dephasing of the binary black holes due to the emission of scalar radiation. This can be traced to the fact that corrections to the scalar amplitude beyond the leading-order decoupling limit scale as the coupling to the third power, which we show here.

In the perturbative approach, the scalar field and tensor field are expanded order by order in a small parameter ϵ,

$$g_{ab} = \sum_{k=0}^{\infty} \epsilon^k g_{ab}^{(k)}, \quad \text{(D1a)}$$

$$\phi = \sum_{k=0}^{\infty} \epsilon^k \phi^{(k)}. \quad \text{(D1b)}$$

We assume $\epsilon \sim \lambda/m_1^2 = \zeta_1$, and set $\phi^{(0)} = 0$, so that the "background" spacetime is vacuum GR. To zeroth order in the coupling, the tensor and scalar equations of motion are

$$G_{ab}^{(0)} - \nabla_a \phi^{(0)} \nabla_b \phi^{(0)} + \frac{1}{2} g_{ab}^{(0)} (\nabla \phi^{(0)})^2 = 0, \qquad \text{(D2a)}$$

$$\Box^{(0)} \phi^{(0)} = 0, \qquad \text{(D2b)}$$

where G_{ab} is the Einstein tensor. We see that if for initial data we set $\phi^{(0)} = \partial_t \phi^{(0)} = 0$, then $\phi^{(0)} = 0$ for all time, and the metric field satisfies the Einstein equations. From now on we assume $\phi^{(0)} = 0$. To linear order in ϵ, the equations of motion are

$$G_{ab}^{(1)} = 0, \qquad \text{(D3a)}$$

$$\Box^{(0)} \phi^{(1)} + \lambda \mathcal{G}^{(0)} = 0. \qquad \text{(D3b)}$$

We see that the equation of motion for $g_{ab}^{(1)}$ is also the vacuum Einstein equations. We can then consistently set $g_{ab}^{(1)} = 0$. The scalar field $\phi^{(1)}$ is no longer zero, even if one initially sets $\phi^{(1)} = \partial_t \phi^{(1)} = 0$ for initial data, as generically $\mathcal{G}^{(0)} \neq 0$. Solving for $\phi^{(1)}$ to this order, while solving for $g_{ab}^{(0)}$ from the Einstein equations, is called the decoupling approximation [38]. To second order in ϵ, we have

$$G_{ab}^{(2)} - \nabla_a \phi^{(1)} \nabla_b \phi^{(1)} + \frac{1}{2} g_{ab}^{(0)} (\nabla \phi^{(1)})^2$$
$$+ 2\lambda \delta_{ijg(a}^{efcd} g_{b)d} (R^{ij}{}_{ef})^{(0)} \nabla^g \nabla_c \phi^{(1)} = 0, \qquad \text{(D4a)}$$

$$\Box^{(0)} \phi^{(2)} = 0. \qquad \text{(D4b)}$$

The scalar equation follows from $g_{ab}^{(1)} = 0$. Note that the scalar equation for $\phi^{(2)}$ would have corrections if the Gauss-Bonnet coupling was nonlinear in ϕ; for more discussion see for example Sec II. B. 5 in [38]. We see that we can consistently set $\phi^{(2)} = 0$. To third order in perturbation theory, we have

$$G_{ab}^{(3)} = 0, \qquad \text{(D5a)}$$

$$\Box^{(0)} \phi^{(3)} + \Box^{(2)} \phi^{(1)} + \lambda \mathcal{G}^{(2)} = 0. \qquad \text{(D5b)}$$

We can set $g_{ab}^{(3)} = 0$, but there is a nontrivial correction to $\phi^{(3)}$ [there would be corrections to $g_{ab}^{(3)}$ if the scalar Gauss-Bonnet coupling was nonlinear in ϕ, due to corrections in $\phi^{(2)}$; see the discussion below Eq. (D4)]. Thus, once one can computed $\phi^{(1)}$, corrections to the scalar waveform do not appear until $\phi^{(3)}$. We considered $\zeta_1 \sim 0.1$ at the largest, so the largest correction due to nonlinear effects to the amplitude would be of relative order $\zeta_1^3/\zeta_1 = \zeta_1^2 \sim 0.01$, a 1% effect. This is consistent with what we see in Figs. 1 and 2.

While nonlinear effects in ζ_1 are not expected to dramatically change the amplitude of the scalar field during inspiral for sGB gravity, nonlinear effects must be incorporated to determine the long-time dephasing of the binary due to the emission of scalar radiation. Nonlinear effects may additionally change the spacetime geometry of the merger in ways not captured in the perturbative approach. Finally, if the scalar Gauss-Bonnet coupling is not linear in ϕ, higher-order corrections in the coupling can enter in the scalar waveform at order ζ_1^2, and so could be more important in determining the properties of black hole binaries.

[1] B. P. Abbott *et al.* (LIGO Scientific, Virgo Collaborations), Phys. Rev. Lett. **116**, 221101 (2016); **121**, 129902(E) (2018).

[2] N. Yunes, K. Yagi, and F. Pretorius, Phys. Rev. D **94**, 084002 (2016),

[3] T. Baker, E. Bellini, P. G. Ferreira, M. Lagos, J. Noller, and I. Sawicki, Phys. Rev. Lett. **119**, 251301 (2017).

[4] B. P. Abbott *et al.* (LIGO Scientific, Virgo Collaborations), Phys. Rev. Lett. **123**, 011102 (2019).

[5] M. Isi, M. Giesler, W. M. Farr, M. A. Scheel, and S. A. Teukolsky, Phys. Rev. Lett. **123**, 111102 (2019).

[6] R. Abbott *et al.* (LIGO Scientific, Virgo Collaborations), arXiv:2010.14529.

[7] M. Isi, W. M. Farr, M. Giesler, M. A. Scheel, and S. A. Teukolsky, Phys. Rev. Lett. **127**, 011103 (2021).

[8] D. Psaltis *et al.* (Event Horizon Telescope Collaboration), Phys. Rev. Lett. **125**, 141104 (2020).

[9] S. H. Völkel, E. Barausse, N. Franchini, and A. E. Broderick, Classical Quantum Gravity **38**, 21LT01 (2021).

[10] P. Kocherlakota *et al.* (Event Horizon Telescope Collaboration), Phys. Rev. D **103**, 104047 (2021).

[11] M. Okounkova, W. M. Farr, M. Isi, and L. C. Stein, Phys. Rev. D **106**, 044067 (2022).

[12] N. Yunes and X. Siemens, Living Rev. Relativity **16**, 9 (2013).

[13] E. Berti *et al.*, Classical Quantum Gravity **32**, 243001 (2015).

[14] E. Berti, K. Yagi, and N. Yunes, Gen. Relativ. Gravit. **50**, 46 (2018).

[15] E. Berti, K. Yagi, H. Yang, and N. Yunes, Gen. Relativ. Gravit. **50**, 49 (2018).

[16] E. W. Hirschmann, L. Lehner, S. L. Liebling, and C. Palenzuela, Phys. Rev. D **97**, 064032 (2018).

[17] M. Okounkova, L. C. Stein, M. A. Scheel, and D. A. Hemberger, Phys. Rev. D **96,** 044020 (2017).

[18] M. Okounkova, L. C. Stein, M. A. Scheel, and S. A. Teukolsky, Phys. Rev. D **100,** 104026 (2019).

[19] M. Okounkova, Phys. Rev. D **102,** 084046 (2020).

[20] J. Cayuso, N. Ortiz, and L. Lehner, Phys. Rev. D **96,** 084043 (2017).

[21] R. Cayuso and L. Lehner, Phys. Rev. D **102,** 084008 (2020).

[22] W. E. East and J. L. Ripley, Phys. Rev. D **103,** 044040 (2021).

[23] J. L. Ripley, Int. J. Mod. Phys. D **31,** 2230017 (2022).

[24] N. Franchini, M. Bezares, E. Barausse, and L. Lehner, Phys. Rev. D **106,** 064061 (2022).

[25] M. Bezares, R. Aguilera-Miret, L. ter Haar, M. Crisostomi, C. Palenzuela, and E. Barausse, Phys. Rev. Lett. **128,** 091103 (2022).

[26] B. P. Abbott *et al.* (LIGO Scientific, Virgo Collaborations), Phys. Rev. D **100,** 104036 (2019).

[27] R. Abbott *et al.* (LIGO Scientific, Virgo Collaborations), Phys. Rev. D **103,** 122002 (2021).

[28] R. Abbott *et al.* (LIGO Scientific, Virgo, KAGRA Collaborations), arXiv:2112.06861.

[29] A. Ghosh (LIGO Scientific–Virgo–Kagra Collaborations), in 56th Rencontres de Moriond on Gravitation (2022), arXiv:2204.00662.

[30] P. Kanti, N. Mavromatos, J. Rizos, K. Tamvakis, and E. Winstanley, Phys. Rev. D **57,** 6255 (1998).

[31] N. Yunes and L. C. Stein, Phys. Rev. D **83,** 104002 (2011).

[32] T. P. Sotiriou and S.-Y. Zhou, Phys. Rev. Lett. **112,** 251102 (2014).

[33] T. P. Sotiriou and S.-Y. Zhou, Phys. Rev. D **90,** 124063 (2014).

[34] K. Yagi, L. C. Stein, N. Yunes, and T. Tanaka, Phys. Rev. D **85,** 064022 (2012); **93,** 029902(E) (2016).

[35] N. Sennett, S. Marsat, and A. Buonanno, Phys. Rev. D **94,** 084003 (2016).

[36] B. Shiralilou, T. Hinderer, S. Nissanke, N. Ortiz, and H. Witek, Phys. Rev. D **103,** L121503 (2021).

[37] B. Shiralilou, T. Hinderer, S. Nissanke, N. Ortiz, and H. Witek, Classical Quantum Gravity **39,** 035002 (2022).

[38] H. Witek, L. Gualtieri, P. Pani, and T. P. Sotiriou, Phys. Rev. D **99,** 064035 (2019).

[39] H. O. Silva, H. Witek, M. Elley, and N. Yunes, Phys. Rev. Lett. **127,** 031101 (2021).

[40] W. E. East and F. Pretorius, Phys. Rev. D **106,** 104055 (2022).

[41] A. D. Kovacs and H. S. Reall, Phys. Rev. Lett. **124,** 221101 (2020).

[42] A. D. Kovacs and H. S. Reall, Phys. Rev. D **101,** 124003 (2020).

[43] L. Aresté Saló, K. Clough, and P. Figueras, arXiv:2208.14470.

[44] J. L. Ripley and F. Pretorius, Classical Quantum Gravity **36,** 134001 (2019).

[45] F.-L. Julié and E. Berti, Phys. Rev. D **100,** 104061 (2019).

[46] F.-L. Julié, H. O. Silva, E. Berti, and N. Yunes, Phys. Rev. D **105,** 124031 (2022).

[47] J. L. Ripley and F. Pretorius, Phys. Rev. D **101,** 044015 (2020).

[48] K. Yagi, L. C. Stein, and N. Yunes, Phys. Rev. D **93,** 024010 (2016).

[49] K. Chamberlain and N. Yunes, Phys. Rev. D **96,** 084039 (2017).

[50] S. E. Perkins, R. Nair, H. O. Silva, and N. Yunes, Phys. Rev. D **104,** 024060 (2021).

[51] Z. Lyu, N. Jiang, and K. Yagi, Phys. Rev. D **105,** 064001 (2022).

[52] F. Pretorius, B. Stephens, and M. W. Choptuik, PAMR, http://laplace.physics.ubc.ca/Group/Software.html.

[53] S. Brandt and B. Bruegmann, Phys. Rev. Lett. **78,** 3606 (1997).

[54] M. Ansorg, B. Bruegmann, and W. Tichy, Phys. Rev. D **70,** 064011 (2004).

[55] V. Paschalidis, Z. B. Etienne, R. Gold, and S. L. Shapiro, arXiv:1304.0457.

[56] V. Paschalidis (private communication).

[57] E. Newman and R. Penrose, J. Math. Phys. (N.Y.) **3,** 566 (1962).

[58] O. J. Tattersall, P. G. Ferreira, and M. Lagos, Phys. Rev. D **97,** 084005 (2018).

[59] P. C. Peters and J. Mathews, Phys. Rev. **131,** 435 (1963).

[60] E. Berti, V. Cardoso, J. A. Gonzalez, U. Sperhake, M. Hannam, S. Husa, and B. Bruegmann, Phys. Rev. D **76,** 064034 (2007).

[61] M. Maggiore, *Gravitational Waves. Vol. 1: Theory and Experiments*, Oxford Master Series in Physics (Oxford University Press, New York, 2007).

[62] D. Christodoulou, Phys. Rev. Lett. **25,** 1596 (1970).

[63] S. W. Hawking, Phys. Rev. Lett. **26,** 1344 (1971).

[64] J. L. Blázquez-Salcedo, C. F. B. Macedo, V. Cardoso, V. Ferrari, L. Gualtieri, F. S. Khoo, J. Kunz, and P. Pani, Phys. Rev. D **94,** 104024 (2016).

[65] L. Pierini and L. Gualtieri, Phys. Rev. D **103,** 124017 (2021).

[66] L. Pierini and L. Gualtieri, Phys. Rev. D **106,** 104009 (2022).

[67] R. Abbott *et al.* (LIGO Scientific, Virgo, KAGRA Collaborations), arXiv:2111.03606.

[68] S. Husa, S. Khan, M. Hannam, M. Pürrer, F. Ohme, X. Jiménez Forteza, and A. Bohé, Phys. Rev. D **93,** 044006 (2016).

[69] S. Khan, S. Husa, M. Hannam, F. Ohme, M. Pürrer, X. Jiménez Forteza, and A. Bohé, Phys. Rev. D **93,** 044007 (2016).

[70] J. T. Gálvez Ghersi and L. C. Stein, Phys. Rev. E **104,** 034219 (2021).

[71] P. Figueras and T. França, Classical Quantum Gravity **37,** 225009 (2020).

[72] P. Figueras and T. França, Phys. Rev. D **105,** 124004 (2022).

[73] A. Dima, E. Barausse, N. Franchini, and T. P. Sotiriou, Phys. Rev. Lett. **125,** 231101 (2020).

[74] C. A. R. Herdeiro, E. Radu, H. O. Silva, T. P. Sotiriou, and N. Yunes, Phys. Rev. Lett. **126,** 011103 (2021).

[75] E. Berti, L. G. Collodel, B. Kleihaus, and J. Kunz, Phys. Rev. Lett. **126,** 011104 (2021).

[76] M. Elley, H. O. Silva, H. Witek, and N. Yunes, Phys. Rev. D **106,** 044018 (2022).

[77] D. D. Doneva and S. S. Yazadjiev, Phys. Rev. Lett. **120,** 131103 (2018).

[78] H. O. Silva, J. Sakstein, L. Gualtieri, T. P. Sotiriou, and E. Berti, Phys. Rev. Lett. **120**, 131104 (2018).

[79] M. Minamitsuji and T. Ikeda, Phys. Rev. D **99**, 044017 (2019).

[80] H. O. Silva, C. F. B. Macedo, T. P. Sotiriou, L. Gualtieri, J. Sakstein, and E. Berti, Phys. Rev. D **99**, 064011 (2019).

[81] W. E. East and J. L. Ripley, Phys. Rev. Lett. **127**, 101102 (2021).

[82] S. Weinberg, Phys. Rev. D **77**, 123541 (2008).

[83] A. D. Kovacs, arXiv:2103.06895.

[84] H.-J. Kuan, D. D. Doneva, and S. S. Yazadjiev, Phys. Rev. Lett. **127**, 161103 (2021).

[85] www.scinethpc.ca.

[86] www.alliancecan.ca.

[87] www.dirac.ac.uk.

[88] W. E. East, F. Pretorius, and B. C. Stephens, Phys. Rev. D **85**, 124010 (2012).

[89] A. H. Mroue, H. P. Pfeiffer, L. E. Kidder, and S. A. Teukolsky, Phys. Rev. D **82**, 124016 (2010).

[90] K. Yagi, Phys. Rev. D **86**, 081504 (2012).

[91] See Supplemental Material at http://link.aps.org/supplemental/10.1103/PhysRevD.107.024014 for calculation of coefficients in Eq. (B8).

[92] G. B. Cook, Living Rev. Relativity **3**, 5 (2000).

[93] L. Blanchet, Living Rev. Relativity **17**, 2 (2014).

[94] K. G. Arun, L. Blanchet, B. R. Iyer, and M. S. S. Qusailah, Classical Quantum Gravity **21**, 3771 (2004); **22**, 3115(E) (2005).